J. Fluid Mech. (1989), *vol.* 203, *pp.* 307–346
Printed in Great Britain

Pressure fluctuations on an oscillating trailing edge

By THOMAS STAUBLI† AND DONALD ROCKWELL

Department of Mechanical Engineering and Mechanics, Lehigh University, Bethlehem, PA 18015, USA

(Received 15 June 1987 and in revised form 18 October 1988)

Turbulent boundary layers separating from a blunt trailing edge give rise to organized vortical structures in the downstream wake. The perturbation of this inherent flow-instability at f_0 by controlled oscillations of the edge at f_e produces corresponding, organized components of unsteady surface pressure along the edge. For edge excitation near the 'natural' vortex shedding frequency f_0, the phase between the local pressure fluctuations and the edge displacement shows large changes for small changes in excitation frequency. Moreover, in this range of excitation, there is quenching (or attenuation) of the surface pressure component at f_0 and resonant peaking of the component at f_e. These phenomena are related to the change in sign of the energy transfer between the fluid and the body. Integration of the instantaneous pressure distributions along the surfaces of the edge leads to the instantaneous lift at f_e and f_0 acting upon the oscillating trailing edge. The location of the lift varies as the cotangent of the dimensionless time during an oscillation cycle. When the edge is excited near, or at, the natural vortex shedding frequency, there is a resonant peak in the amplitude of oscillation of the lift location at f_e; that at f_0 is invariant. Moreover, the mean location of the lift at f_e undergoes abrupt changes in this region of excitation. Flow visualization allows determination of the phasing of the organized vortical structures shed from the trailing edge relative to the edge displacement. Modulation of the flow structure at the frequencies f_0 and f_e, as well as interaction of small-scale vortices at high excitation frequencies, was observed. These aspects of the near-wake structure are related to the instantaneous pressure field.

1. Introduction

The formation of vortex streets from streamlined bodies having blunt trailing edges is a major source of flow-induced vibration and noise generation. The nature of vortex formation is assessed by Wood (1971), Brepson & Leon (1972), Greenway & Wood (1973), Blake (1984) and Graham & Maull (1971). This class of vortex formation from blunt trailing edges is akin to the extensively investigated vortex formation from cylinders. The investigations and overviews of Roshko (1954), Abernathy & Kronauer (1962), Morkovin (1964), Bearman (1967, 1984), Berger & Wille (1972), Griffin & Ramberg (1974), Gerrard (1978), Sarpkaya (1979) and Saffman & Schatzman (1982) provide a perspective on the wide variety of issues associated with this class of flows, beyond the scope of this Introduction.

The overall purpose of this investigation is to focus on the unresolved issues of surface loading and near-wake flow structure that are inherent to vortex formation from both blunt trailing edges and cylindrical bodies. The configuration of the blunt

---

† Present address: Sulzer Escher Wyss AG, Hydraulik CH-8023 Zürich, Switzerland.

trailing edge provides particularly well-posed experimental conditions: fixed separation points at the separation edge; a forward stagnation point located far upstream of the trailing edge; and a fully developed flow separating from the trailing edge, subjected to a zero streamwise pressure gradient upstream of the edge.

The first issue for this class of flows is the loading on the surface of the edge as a function of the frequency of the edge motion. For example, it is known that when the trailing edge is subjected to controlled oscillations at a frequency near the natural vortex shedding frequency, there occurs a drastic shift in phase of the pressure (at a location near the corner of the edge) relative to the edge displacement (Blake & Maga 1979). Analogous phase shifts of the lift or pressure occur for flow past a square cylinder (Bearman & Obasaju 1982) and flow past a circular cylinder (Bishop & Hassan 1964; Jones 1968; Sarpkaya 1978; Bearman & Currie 1979; Staubli 1981). These changes in phase are accompanied by the occurrence of a resonant (amplitude) peak of the fluctuating pressure or lift. All of the foregoing investigations have focused on measurement of either pressure at a single location or gross lift acting on the surface. An overall objective of the present investigation is to gain a fuller understanding of the surface loading by obtaining instantaneous pressure distributions over the entire surface of the trailing edge while the edge is undergoing controlled oscillations at various values of prescribed frequency. This approach will reveal: the regions of the localized surface loading that make the largest contributions to the instantaneous lift; time-dependent variations of the location of the resultant lift acting on the surface; the relative contributions to the local pressure fluctuations from the instabilities due to the edge forcing as well as to the inherent vortex formation; the relative magnitudes of the pressure fluctuations without and with mean flow past the trailing edge; and the relation of all of these features to the phase shift and the amplitude at resonance of the gross loading of the surface.

The second issue to be addressed is alteration of the near-wake flow structure. The vortex formation process leading to the Kármán vortex street is known to be a highly organized, self-excited instability. The manner in which this vortex formation responds to perturbations of various frequencies is not adequately understood. Moreover, the relationship between the alteration of the vortex formation process and the foregoing aspects of the force and pressure loading on the edge is an essential, unresolved matter. The importance of investigating this aspect is suggested by the hypothesis of Zdravkovich (1982): the phase shift of the lift on a cylinder is accompanied by a change in timing of the vortex shedding with respect to the cylinder displacement. This observation has been addressed recently by Ongoren & Rockwell (1988). A further objective of this investigation is, therefore, to correlate the visualized patterns of instantaneous vortex shedding with the instantaneous position of the edge and the corresponding instantaneous surface pressure distributions. Particularly important will be determination of how the instantaneous vortex formation process is related to the phase shift of the loading through the synchronization range.

2. Experimental facility and instrumentation

2.1. *Overview of design considerations*

The primary design consideration is to provide a means of generating a well-defined bluff-body vortex street. The configuration should be a generic one and allow control and interpretation of the flow structure and the corresponding surface pressure loading with a minimum of complicating influences. A blunt trailing edge has fixed

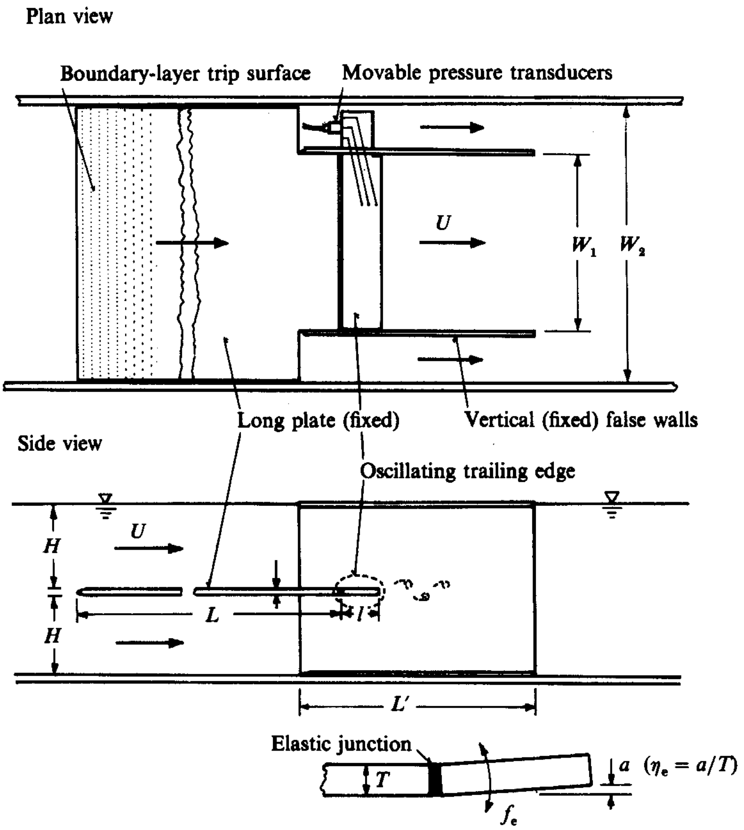

FIGURE 1. Plan and end views of test section housed within water channel. Long plate allows fully developed turbulent boundary layer. Oscillating trailing end is subjected to oscillations at controlled frequency and amplitude.

separation points; moreover, the upstream stagnation point is located far upstream of the trailing edge and therefore does not undergo significant oscillations. Further, the flat plate upstream of the trailing edge provides a means of generating a fully developed turbulent boundary layer in a zero streamwise pressure gradient. All of these considerations allow more simplified experimental conditions than the classical geometry of the cylinder.

The flat plate with an oscillating trailing edge is indicated in figure 1. The total length $L+l$ of this plate configuration allowed attainment of a fully developed turbulent boundary layer at the trailing edge. The plate length $L+l$ was 1500 mm and the corresponding Reynolds number $Re_L = 3.6 \times 10^5$. To ensure that a fully turbulent flow condition was attained, the boundary layer was tripped at the leading edge of the plate as described subsequently. The momentum thickness θ of the boundary layer at the trailing edge, relative to the trailing-edge thickness T (i.e. θ/T), must lie in a range that promotes coherent formation of the vortex street in the near wake. Linear stability theory provides guidelines for determining the optimum ratio of θ/T (Monkewitz & Nguyen 1987). Suitable conditions for this experiment corresponded to $Re_\theta = 940$ and $\theta/T = 0.156$.

Regarding the excitation parameters of the trailing edge, the excitation frequency f_e must be considered relative to the inherent vortex shedding frequency f_0^* from the stationary edge. Since $f_0^* = 1.95$ Hz, values of excitation frequency $0.5 \leqslant f_e \leqslant 6$ Hz were selected, corresponding to a range of frequency ratios $0.25 \leqslant f_e/f_0^* \leqslant 3.08$, thereby providing a range of excitation frequencies below and above the anticipated synchronization at or near $f_e/f_0^* = 1$. Considerations in determining the excitation amplitude $\hat{\eta}_e$ are: it should be small enough to avoid multifrequency components in the pressure signals due to strong nonlinearities in the response of the flow instability; and large enough to ensure a measurable range of synchronization of the flow structures to the edge motion. Accounting for these considerations, as well as the resolution of the measuring system, the optimum values of displacement amplitude of the trailing edge were ±0.25 and ±0.5 mm. The corresponding normalized amplitudes, relative to the trailing-edge thickness $T = 25$ mm, were $\hat{\eta}_e = 0.01$ and 0.02.

2.2. *Flow facility*

The experiments were carried out in a newly constructed, large-scale water channel. This free-surface channel was designed for investigation of instability-type experiments. It allows simultaneous velocity and pressure measurement in conjunction with flow visualization. The entire channel system is constructed of plastic, with the exception of the brass pump, to preclude corrosion that is inevitable during the electrolysis process employed in flow visualization. The side and bottom walls of the test section are made of Plexiglas, in order to facilitate flow visualization from arbitrary views. The length of the test section is 4 m with a cross-section of 0.6 m × 0.9 m.

Water is recirculated by a 10 in. axial flow pump, located 5 m below the free surface in a separate chamber beneath the test section of the water channel. The desired flow speeds are achieved by a controlled, variable-frequency power supply to the motor. The maximum achievable discharge with the installed motor was 0.15 m^3/s. Before entering the test section, the water passes through different flow manipulators and a carefully designed contraction in order to minimize turbulence effects in the test section.

The pump was separated from the water channel by a 200 mm thick concrete floor in order to reduce transmission of vibration. To further provide vibration isolation, piping from the intake and from the suction and pressure sides of the pump was connected with a flexible rubber coupling. In investigations of flow instabilities of interest herein, it is essential that the resonant frequencies of the entire test section are known. They must be well separated from the investigated excitation frequencies of the flow instabilities, which were in the range of 0.5 to 6 Hz. Preliminary transient response tests indicated a resonant frequency at 9 Hz. Since this vibration had its origin in the stiffness of the frame supporting the test section and the mass of water in the test section, it was straightforward to raise this frequency to about 15 Hz by stiffening the support structure.

2.3. *Test section insert and edge forcing system*

The test section insert for the present experiments was placed within the main test section of the channel, as indicated in figure 1. This insert included a $T = 25$ mm thick plate of $L+l = 1.5$ m length, with trailing-edge length $l = 125$ mm, and a four-sided box containing the oscillating trailing edge with its pressure taps. The purpose of this box, which covered the free water surface, was to minimize wave effects on the formation of the wake behind the trailing edge. Further, this box provided essentially two-dimensional flow conditions approaching the trailing edge by clipping off the sidewall boundary layers of the channel. The box was $L' = 0.79$ m

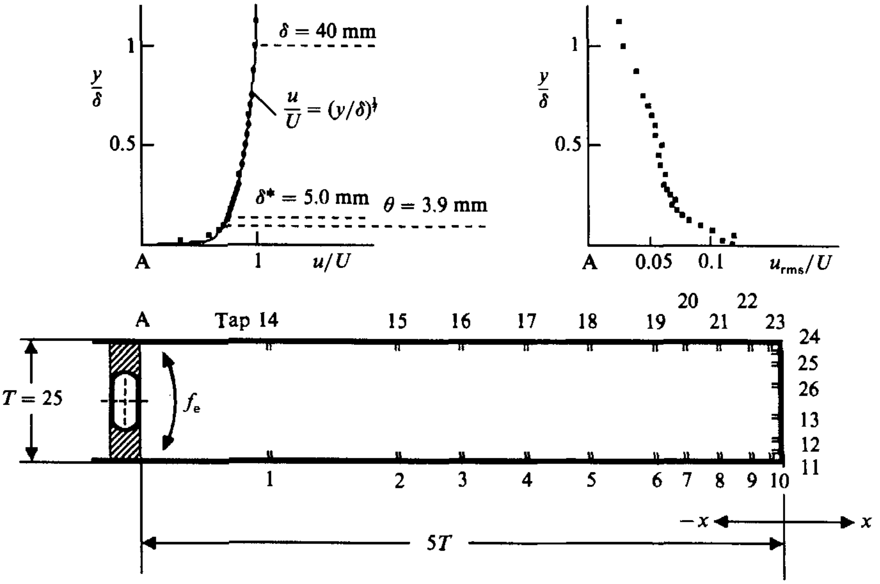

FIGURE 2. Cross-sectional (side) view of trailing end (compare with figure 1) showing locations of elastic junction (at A) and pressure taps along surface. Velocity distributions within the boundary layer above point A are also illustrated.

long, $2H+T = 0.56$ m high and $W_1 = 0.6$ m wide, relative to the channel width $W_2 = 0.9$ m.

The approach flow impinged upon the long plate; its leading edge, with a boundary-layer trip section, was designed in accordance with the findings of Johansen & Smith (1983). The artificial surface roughness extended downstream of the leading edge over a distance of 180 mm and contained 9 rows of particles with a streamwise spacing of 19 mm. The upstream rows were particles having a typical size of 2 mm with a spacing of 9.5 mm, and the downstream rows were particles having a typical size of 4 mm and a spacing of 19 mm.

Particular care was given to the manufacture of the flexible connection between the long plate and the oscillating trailing edge, indicated in figure 2. The central portion of this junction was made of tygon tubing; in the cross-hatched region, silicon rubber was inserted, and a smooth finish was obtained on the surface by shaping the interface after drying. This flexible joint was compressed together by several long, flexible screws, which connected the oscillating edge with the fixed plate. Two needle-type bearings at either end of the oscillating edge provided an effective bearing for the pivoted motion of the edge; this bearing system allowed adjustment of the axis of rotation to the centre of the elastic junction.

At this point, it is appropriate to consider the concept of externally forcing the trailing edge, as opposed to letting it vibrate freely. When the body or edge oscillates, there is potentially strong coupling between the body motion and the flow structure in the near wake. In practice, these body oscillations arise from an elastically mounted, or flexible, body. However, one can simulate certain features of this phenomenon by subjecting the body to controlled forcing. Bearman (1984) assesses the possibility of inferring the response of the self-excited (elastic) body from the corresponding externally controlled body. In general, controlled-excitation experiments are relevant to self-excitation of the corresponding elastic system. For identical steady-state motion of the body, we expect the same flow structure to occur in the case of controlled or of self-excited oscillations of the body. In fact, Staubli (1981) interprets his experiments on controlled excitation of a cylinder, via appropriate computations, to the amplitude response of the self-excited experiments of Feng (1976); the principal features, including hysteresis effects, are well simulated.

The trailing edge was driven by a custom-designed forcing mechanism that allowed oscillation amplitudes of the tip of the edge as low as 0.1 mm to be obtained. The forcing mechanism consisted of a controlled, variable-speed DC-motor and a cam arrangement. This cam arrangement was designed such that even the smallest amplitudes of oscillation could be reproduced with an accuracy of better than 1%. The displacement, which was mechanically amplified with an elongated lever arm, was in turn measured with a linear potentiometer. The connection between the cam arrangement and the trailing edge was a vertical rod, which was pointed at both ends and mounted in needle-type supports. An initial bias force ensured tight contact between the tips of the vertical rod and the supports, even at the very high frequencies of oscillation. The drive and the trailing edge were stiff enough to avoid any feedback of the fluid forces on the motion of the driven body, thereby maintaining purely sinusoidal motion.

Besides clipping off the boundary layers along the sidewalls of the channel, the gap between the test section insert box and the channel walls (see figure 1) allowed isolation of the vertical driving rod of the edge forcing mechanism on one side, and pressure transducers on the other side. That is, there was no interference with the flow passing through the test-section insert. The driving rod and pressure transducers were mounted on opposite sides of the trailing edge in order to avoid deformation of that part of the trailing edge that housed the channels leading to the pressure transducers. The pressure transducers were mounted close to the axis of rotation of the trailing edge where acceleration effects on the transducers and on the connecting cables are minimal.

2.4. *Pressure and velocity measurements*

Fluctuating pressure was measured at the 26 pressure taps schematically shown on the cross-section of the trailing edge in figure 2. These taps consisted of 0.5 mm diameter holes having a depth of 3 mm; they were connected to 2 mm channels machined in the edge, and led to the sensing face of the transducers. Only two pressure transducers were employed; they simultaneously measured pressures on the upper and the lower surfaces of the edge. These transducers were switched successively during the measurements to all 13 pairs of pressure tap connections. Before measurements, the pressure lines were purged of air bubbles with an air-ejector pump. The resonant frequency of the tap–channel–transducer system was well above 100 Hz as ascertained by transient tests; this frequency is sufficiently high so as not to affect significantly the amplitude and phase of the pressure fluctuations for the frequency range of interest herein.

Pressure measurements were carried out using two Kulite XCS-190 transducers, coated with a parelene film in order to avoid corrosion of the sensitive face. Calibration of the pressure transducers and recalibration after measurements showed a repeatability of better than ±1%. From the scatter of the measured amplitudes and from redundant measurements on the lower and upper surfaces an overall accuracy of better than ±5% can be estimated – except for the spectral components having very small amplitudes, where the relative error might be higher; such small amplitudes occur in the case of quenched, self-sustained pressure fluctuations (e.g. see figure 8*c*). The drift of the semiconductor-type pressure transducers and the attached differential amplifiers (Tektronix) was small enough to allow static calibration of the transducers. However, this drift was too large to allow determination of the small changes in the mean static pressure along the surfaces of the trailing-edge. The following discussions of measurements and errors, therefore, are restricted to contributions due to deterministic pressure fluctuations upon the edge.

By making redundant measurements on the lower and upper surfaces it was possible to check symmetry conditions (π phase shift) and to average the results. The maximum deviation of the lower and upper pressure amplitudes with respect to the averaged value was $\pm 5\%$; in general it lay between $\pm 2\%$.

Experiments were performed at a free-stream velocity $U = 0.242$ m/s, and a Reynolds number based on the plate length of $Re_L = 3.6 \times 10^5$. Detailed boundary-layer traverses were carried out at location A, indicated in figure 2. It is important to emphasize that there is substantial distortion of the mean and fluctuating velocity fields as well as the mean static pressure distribution (Blake 1984*a, b*; Unal & Rockwell 1988) in the vicinity of the trailing end. In order to ensure that the characteristics of the turbulent boundary layer were not contaminated by the changing boundary conditions at the trailing end, the measurements were carried at the flexible junction located five trailing-edge thicknesses upstream from the trailing end. These velocity measurements were performed using a DISA-hot-film anemometer system. Linearization of the signals was performed after A/D conversion of the amplifier outputs on a PDP-11/23, using a fifth-order polynomial approximation of the calibration curve of the hot-film probe. The mean velocity distribution, whose outer region is represented in figure 2, was well fitted by a $\frac{1}{7}$ power distribution. The exponent $\frac{1}{7}$ was determined from a linear fit of the mean velocity distribution on double-logarithmic coordinates. The boundary-layer thickness $\delta = 40$ mm is defined by $U(\delta) = 0.99U$. The Reynolds number based on the momentum thickness $\theta = 3.9$ mm was $Re_\theta = 940$. Regarding the turbulence intensity, its distribution was essentially equivalent to that obtained by Johanson & Smith (1983), Schlichting (1979) and Purtell & Klebanoff (1981) for fully developed turbulent boundary layers at low Reynolds numbers Re_θ. In making these comparisons, measurements in addition to those of figure 2 were plotted on semilogarithmic coordinates, confirming the agreement with the logarithmic law of the wall.

All displacement, pressure and velocity signals were digitized and processed by a PDP 11/23 computer. Power spectral density distributions and cross-spectral density distributions were evaluated, from which the amplitudes and phases of the spectral components of deterministic contributions to the signal at different frequencies were determined. For each measuring point and parameter set, several ensembles of 512 digitized points were compared and averaged in the frequency domain. The chosen window was of the Hanning type and the analysis band for frequencies ranged, in general, from 0 to 12 Hz. Aliasing was avoided by appropriate filtering. In preliminary investigations, ensembles of 1024 sampling points and larger frequency ranges were investigated.

2.5. *Flow visualization*

Flow visualization was carried out using the hydrogen bubble technique whereby a 0.075 mm diameter platinum wire was mounted vertically at a distance of 2 mm downstream from the trailing end. By employing pulsed timeline markers, it was possible to visualize the phase speed and the rate of development of the coherent vortical structures shed from the trailing edge. Effective illumination was achieved by use of one 1000 W powered stroboscopic light of 15 ms flash duration in conjunction with two 90 W strobe lights for illumination of the shadow regions. The time records of the flow patterns were recorded with a video camera at a rate of 120 frames per s. All components of the video and lighting system were manufactured by Instar Corporation. By employing a photodiode arrangement flashing at the uppermost position of the oscillating edge during its oscillation cycle, and by recording these flashes simultaneously on the video, it was possible to relate the phasing of the observed vortical structures to the displacement of the oscillating trailing edge. This procedure, in turn, allowed determination of the phasing of the instantaneous flow structure in the vicinity of the trailing end and the pressure fluctuations upon the surface of the trailing edge.

In preliminary experiments, flow visualization was performed to check the parallelism of vortex shedding with respect to the trailing end. For this purpose a long, horizontal wire of stainless steel, 0.025 mm diameter, was oriented with its axis parallel to the trailing end. This wire did not give the same excellent bubble quality as was achieved with platinum wire, but its higher strength allowed it to be stretched over a long distance at high tension in order to avoid deformation by the flow. These experiments showed that the correlation along the span is highly sensitive to upstream distortions. For example, small air bubbles trapped in the honeycomb (located in the upstream plenum) could cause small upstream flow asymmetries which, in turn, could cause vortex shedding at an angle relative to the trailing end; this type of asymmetry, which may have additional causes as well, has been reported in many experiments on vortex shedding behind circular cylinders (Berger & Wille 1972). Once these upstream influences were eliminated, there was excellent parallelism, in the time mean, of the cores of shed vortices relative to the trailing end over at least three-quarters of the span; the outer regions were influenced by inevitable endwall effects.

3. Pressure loading upon the stationary edge

Turbulent boundary layers give rise to broadband pressure fluctuations on stationary surfaces. The spectral content of the surface pressure on a flat plate (well away from its trailing edge) has been characterized recently by Schewe (1983). Preliminary experiments showed that these turbulence-induced contributions to the power spectral density of the pressure were at least two orders of magnitude smaller than the deterministic contributions due to periodic vortex shedding in vicinity of the trailing end. For this reason, and because of the primary focus on vortex shedding phenomena in this investigation, only narrowband analysis of the deterministic contributions was considered. These deterministic contributions are in the form of nearly sinusoidal pressure fluctuations, as evident from time-dependent oscilloscope traces and from the discrete peaks observed in the power spectral density distributions. We note that this self-generated coherence in the near wake is in contrast to that observed for turbulent flow from a thin trailing edge or certain bevelled trailing edges (Blake 1984*b*). In fact, a turbulent mixing layer from a thin trailing edge generates highly organized flow structures only when it is subjected to substantial acoustic forcing (Fiedler & Mansing 1985).

Figure 3 shows the phase and amplitude distributions of the fluctuating pressure as a function of distance from the trailing end. The corner of the trailing end is

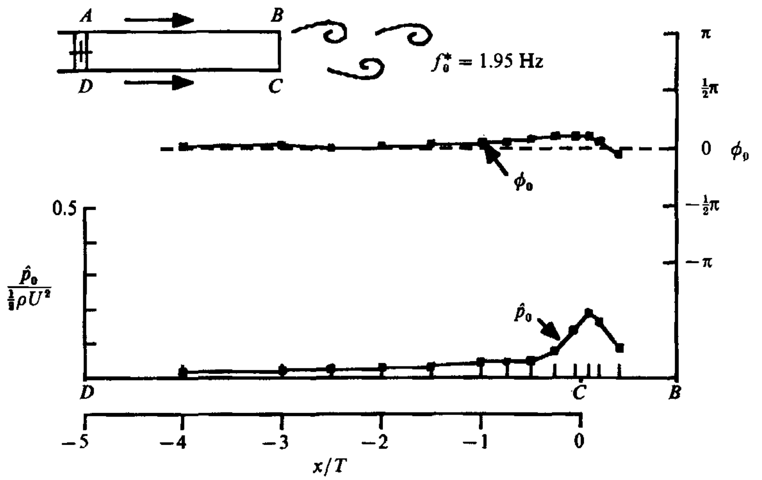

FIGURE 3. Amplitude and phase distributions of pressure fluctuations induced by 'natural' vortex shedding ($S_0^* = 0.2$) in the absence of edge oscillations.

located at $x/T = 0$ and the upstream end of the flexible trailing edge is at $x/T = -5$. Note that the vertical surface at the trailing end, i.e. the base BC, has been projected onto the horizontal axis.

According to our experimental observations, the deterministic contribution $p_0(x,t)$ to the pressure fluctuations at the fundamental frequency f_0^* of the natural vortex shedding can be written, to a good approximation, as follows:

$$p_0(x,t) = \hat{p}_0(x)\cos\{2\pi f_0^* t + \phi_0(x)\}. \tag{1}$$

The frequency of the natural shedding in the absence of edge oscillations is $f_0^* = 1.95$ Hz, which corresponds to a Strouhal number based on the trailing-edge thickness of $S_0^* = 0.2$; basing the Strouhal number on the trailing-edge thickness plus two momentum thicknesses gives $S_{2\theta} = 0.26$.

The phase $\phi_0(x)$, displayed in figure 3, is defined with respect to the pressure fluctuations at the furthest upstream tap on the lower surface, which is at $x/T = -4$. We see that there is a rather small phase gradient $\mathrm{d}\phi_0(x)/\mathrm{d}x$ as we approach the trailing end; upstream of this region there is practically zero phase gradient. This demonstrates that the pressure fluctuations far enough upstream of the trailing end are not caused by convective effects but rather originate from the upstream influence of the shed vortices. Physically, a zero phase gradient means that the pressure fluctuations are felt everywhere simultaneously; or, more precisely, since the lengthscale of the trailing edge is very small compared to the wavelength of sound waves, the phase shifts at a distance of two trailing-edge thicknesses upstream of the trailing end are too small to be measured. Concerning the phase on the upper surface of the trailing edge, we measured a phase difference of $\pi \pm 0.05$ rad with respect to the fluctuations on the lower surface.

The positive gradient of $\phi_0(x)$, $\mathrm{d}\phi_0(x)/\mathrm{d}x$, upstream of the corner suggests an upstream-travelling pressure wave, if one restricts interpretation of the near-wake instability to a purely convective one. This would mean that there is propagation of information from the corner of the edge to a region upstream of it. However, recent analyses of the near-wake instability of bluff-body configurations, assessed by Monkewitz & Nguyen (1987), show that an absolute, as opposed to a convective,

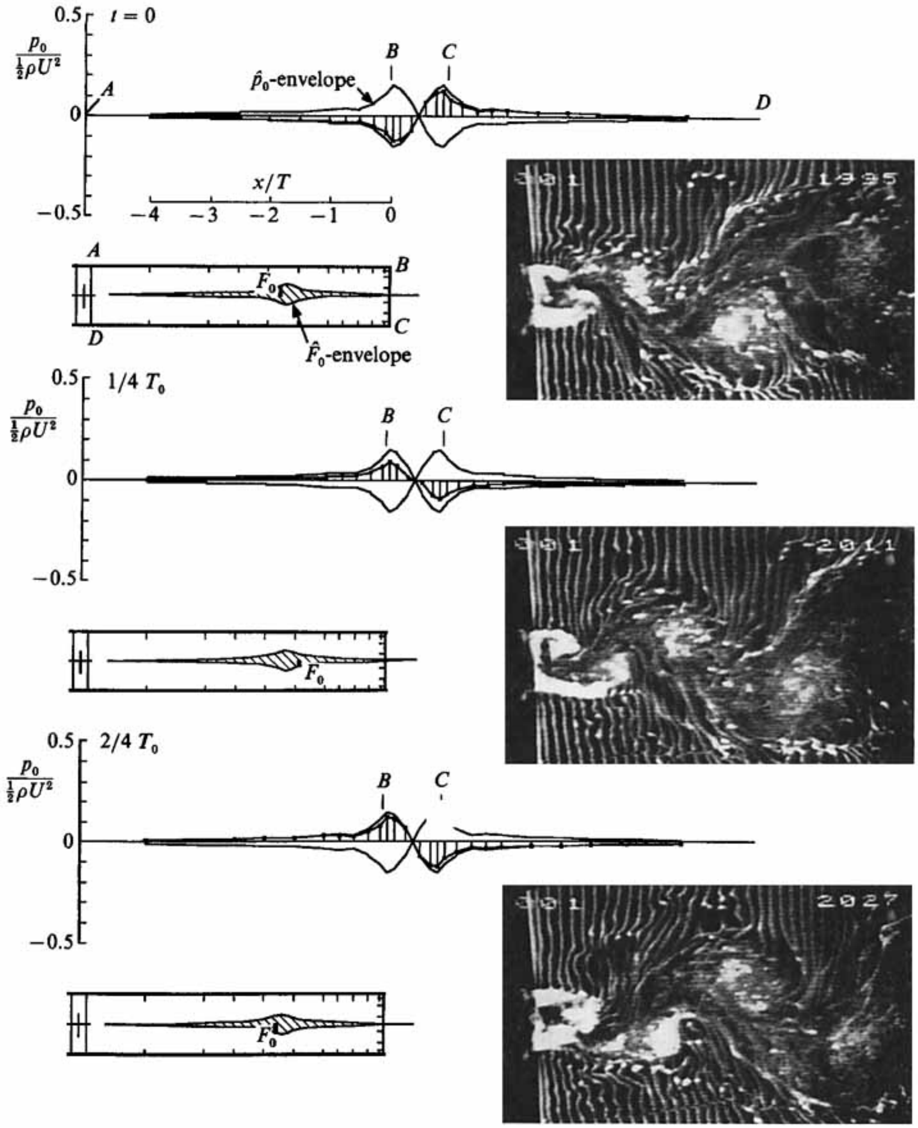

FIGURE 4. For caption see facing page.

instability can exist in the near wake. The important feature of this type of instability is that there can be both downstream and upstream waves coexisting in the near wake. For the purpose of interpreting the surface pressure fields considered herein, it is essential to recognize that all absolute instability analyses of the near wake do not account for the presence of the body. Therefore, it is difficult to establish the link between the absolute instability of the near wake and the type of fluctuating pressure distribution on the surface. Clearly, further analytical studies are needed to establish the relation between the sign (positive or negative) of the streamwise phase gradient of pressure and the possible upstream transmission of pressure fluctuations.

The amplitude $\hat{p}_0(x)$ of the pressure fluctuations upon the stationary edge evidently has a maximum near the corner of the edge. The decay upstream of the corner at C (or B) can be empirically approximated by $\hat{p}_0(x) = \hat{p}_0(C)/(|1-4x/T|)$. It

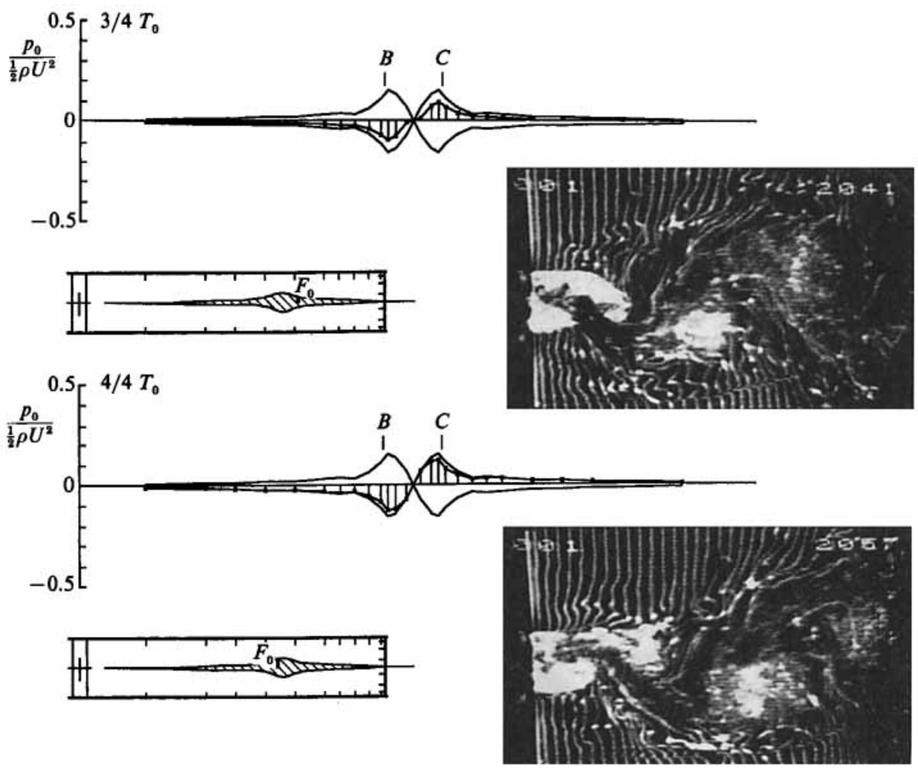

FIGURE 4. Time sequence of the flow structure and the corresponding instantaneous pressure field for the stationary trailing edge. $Re_L = 3.6 \times 10^5$; $Re_\theta = 940$; $S_0^* = 0.2$ (at each instant of time, the spatial distributions of force and pressure are illustrated). Force $\hat{F}_0$ amplitude envelope (cross-hatched region) and location (vertical bar) are depicted within the cross-section of the trailing edge. Distributions of the pressure $\hat{p}_0$ amplitude envelope (solid line) and instantaneous distribution (vertical bars at location of pressure taps) are indicated.

is clearly inappropriate to assume the existence of a Kutta condition at the trailing edge. Simply put, the pressure amplitude would have to go to zero (over a distance commensurate with the lengthscale of the edge) as the corner of the edge is approached (D. G. Crighton 1986, private communication). The pressure amplitude distribution of figure 3 exhibits quite the opposite behaviour. Furthermore, we note the lack of a discontinuity in the pressure distribution around the corner; this observation is confirmed by all measurements with the oscillating trailing edge, to be addressed subsequently.

The approximation for the pressure fluctuations of equation (1) neglects contributions due to higher harmonics, especially that at $2f_0^*$. Generally, these contributions were smaller than 20% of the fundamental, even for the pressure taps on the vertical trailing end, with exception of the two taps close to the midpoint of the trailing end. Here the component at $2f_0^*$ reached amplitudes comparable with that of the fundamental. For the midpoint of the trailing end, however, it can be concluded from interpolation of the taps just above and below that location (there was no tap exactly in the centre) as well as from symmetry considerations, that the contribution due to the frequency f_0^* will disappear in the centre; the contributions due to $2f_0^*$, in contrast, will not disappear and therefore will locally dominate the pressure fluctuations at this midpoint of the trailing end. This observation that the second harmonic is not necessarily dominant in the whole base region somehow contradicts the findings of Blake (1984*a*, *b*) and others who report only contributions due to the second harmonic at $2f_0^*$.

A time sequence of the flow structure for the stationary trailing edge and the corresponding instantaneous pressure field is shown in figure 4. Successive photos are separated by one-quarter of the self-excited period $T_0^* = 1/f_0^*$ of the natural vortex shedding. From the flow visualization, it is evident that organized vortical structures emerge from the background turbulence of the approach boundary layer. The basic flow structure repeats after one cycle, as is evident in the fifth photograph. If one tracks, starting with the top photo, the development of the vortices shed from the bottom and top corners of the trailing edge, then it is evident that the distance between the fronts of these vortices drastically increases, until the wavelength of the classical vortex street is obtained sufficiently far downstream of the end. This asymptotic wavelength corresponds to approximately 4 trailing-edge thicknesses. This drastic increase in wavelength in the vortex formation region is associated with corresponding changes in phase speed, since the frequency remains constant. In this region, the mean flow is highly non-parallel.

The drawings on the left side of the photographs of figure 4 show the corresponding pressure distributions. They include the envelope $\hat{p}_0$ of the pressure fluctuations already given in figure 3. The pressures on the vertical trailing end (*B*–*C*), as well as the pressures on the lower surface (*C*–*D*) are projected onto the same horizontal axis as those of the upper surface (*A*–*B*). These instantaneous pressure fluctuations are indicated by vertical markers. Moreover, within the schematic of the trailing edge, there is depiction of the amplitude of the resultant, instantaneous force $F_0(t)$ at its instantaneous location, represented by a bold, vertical bar. The time-averaged amplitude envelope of this resultant force, which was determined from integration of the instantaneous pressure distribution along the surface of the trailing edge, is indicated by the shaded area. The force location followed from determination of the instantaneous torque about the flexible joint of the trailing edge. Since periodic variation of the instantaneous force passes through zero twice during one cycle of edge oscillation and since the point of application results from division of torque by force (see equations (8), (9) in §7), we expect two singularities for the time-dependent point of force application. Note that the envelope of the force F_0 is truncated on both ends; its extremes actually extend to ±infinity as the force $F_0(t)$ goes to zero. Details of the force amplitude and its instantaneous point of application will be discussed in §7.

Comparing the top row of flow visualization and the instantaneous pressure and force schematics, it is evident that the force is maximum-positive when the vortex starts forming at the upper corner ($t/T_0^* = 0$). At this instant it induces maximum negative pressure in the region near the upper corner. The identical situation occurs at the bottom corner for $t/T_0^* = \frac{1}{2}$. This phase shift of a half-cycle for flow events occurring on the upper and lower surfaces of the edge, which is in accord with the π phase shift of the instantaneous pressures, demonstrates the antisymmetrical character of the flow field. Regarding the pressure fluctuations on the trailing end, or base, it is evident that the pressure amplitude at frequency f_0^* goes to zero midway between *B* and *C*. It is at this point that the fluctuations at $2f_0^*$, not shown, have their local maximum amplitude.

4. Unsteady pressure field in the absence of a mean flow

Before considering the loading on an oscillating edge in mean flow, it is instructive to consider the corresponding case without flow. When the trailing edge undergoes forced oscillations of small amplitudes in still water, there will be a non-circulatory or 'added mass' contribution to the pressure fluctuations due to the displacement of the surrounding fluid (Bisplinghof, Ashley & Halfman 1955). From simple non-circulatory considerations, we expect the amplitudes of the induced pressures to vary linearly with increased amplitude of oscillation and to be proportional to the square of the frequency of oscillation; furthermore, we expect no phase shift along the upper and lower surfaces and a phase shift of π between the upper and the lower surface.

Since the distance of the trailing end to the axis of rotation was 250 times larger than the maximum investigated amplitude of oscillation, the motion of the trailing edge can be described by the vertical displacement a of the tip:

$$\eta(t) = \frac{a}{T}\cos 2\pi f_e t = \hat{\eta}_e \cos 2\pi f_e t, \tag{2}$$

where a is the amplitude of tip displacement, and f_e is the frequency of external excitation.

The pressure fluctuations along the trailing-edge surface can be written, neglecting higher harmonics, as follows:

$$p_e(x,t) = \hat{p}_e(x)\cos\{2\pi f_e t + \phi_e(x)\}, \tag{3}$$

in which $\phi_e(x)$ is the measured phase shift between the pressure fluctuations at location x and the edge displacement.

Figures 5 and 6 show, in three-dimensional plots, the amplitude $\hat{p}_e$ and the phase ϕ_e as a function of excitation frequency f_e, as well as location along the surfaces *D–C* (lower surface) and *C–B* (vertical base); note that the vertical surface *C–B* is projected onto the same horizontal axis as surface *D–C*. Detailed examination of the data corresponding to the plots of figures 5(*a*) and 5(*b*) showed that, for each location, pressure $\hat{p}_e$ increases basically linearly with increasing $\hat{\eta}_e$ and is proportional to f_e^2, within experimental uncertainty. This trend also holds for higher excitation frequency f_e, as will be discussed in conjunction with figure 8(*a*). Figure 5 shows that the maxima of the pressure amplitudes occur about 1.5 trailing-edge thicknesses upstream from the trailing end.

Figures 6(*a*) and 6(*b*) show the phase distributions corresponding to the amplitude data of figures 5(*a*) and 5(*b*). Both distributions are practically identical and confirm the expected zero phase relative to the displacement signal along the surfaces. Only the pressure tap close to the midposition of the vertical trailing end showed a distinct phase shift of π. This rather surprising result can be understood from examination of a time sequence of the instantaneous pressure distribution for edge oscillations in still water, which is displayed in figure 7. This jump of π is most likely associated with the onset of substantial viscous effects and secondary flows at the midsection of the base.

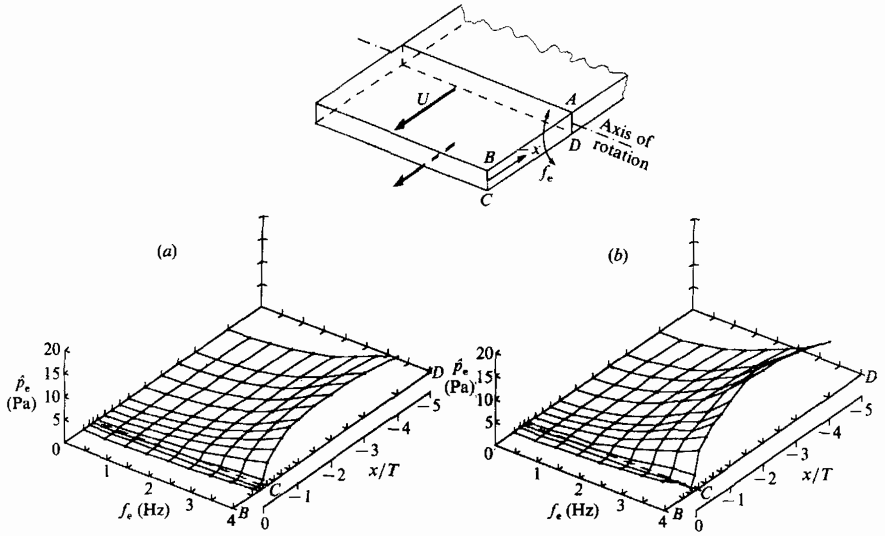

FIGURE 5. Amplitude $\hat{p}_e$ of the pressure fluctuations for edge oscillations in still water showing: (a) oscillation at amplitude $\hat{\eta}_e = 0.01$; and (b) $\hat{\eta}_e = 0.02$.

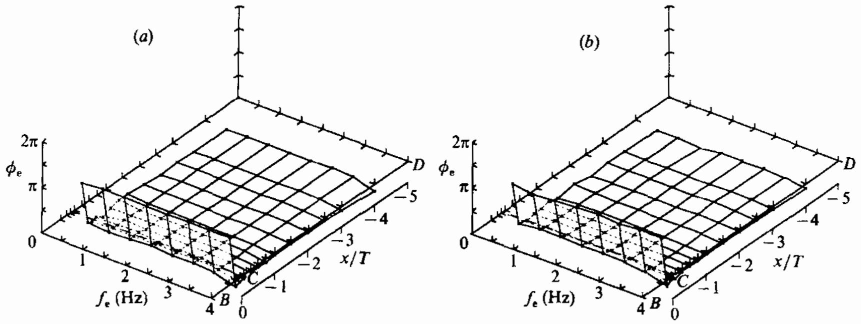

FIGURE 6. Phase angle ϕ_e between the pressure fluctuations $p_e(t)$ and the edge displacement $\eta_e(t)$ for oscillations in still water showing: (a) oscillation at amplitude $\hat{\eta}_e = 0.01$; and (b) $\hat{\eta}_e = 0.02$.

5. Unsteady pressure field in the presence of mean flow

5.1. *Basic features*

The response of the flow field to controlled sinusoidal displacement of the trailing edge was investigated by varying the excitation frequency. Because of the nonlinearity of this response, two different amplitudes of oscillation were investigated.

In general, the response can be approximated as the superposition of two fluctuations: one at the frequency f_e of external excitation; and the other at the frequency f_0 of the self-excited vortex shedding. In flow visualization, this superposition appears as a modulation of the flow structure with a period corresponding to $|1/f_e - 1/f_0|$. For the pressure signals, we observe a similar modulation in the time records. The Fourier transform of the pressure signals reveals that this modulation in the time domain is a combined phase and amplitude modulation due to the superposition of two sinusoidal contributions at f_0 and f_e, each having its own

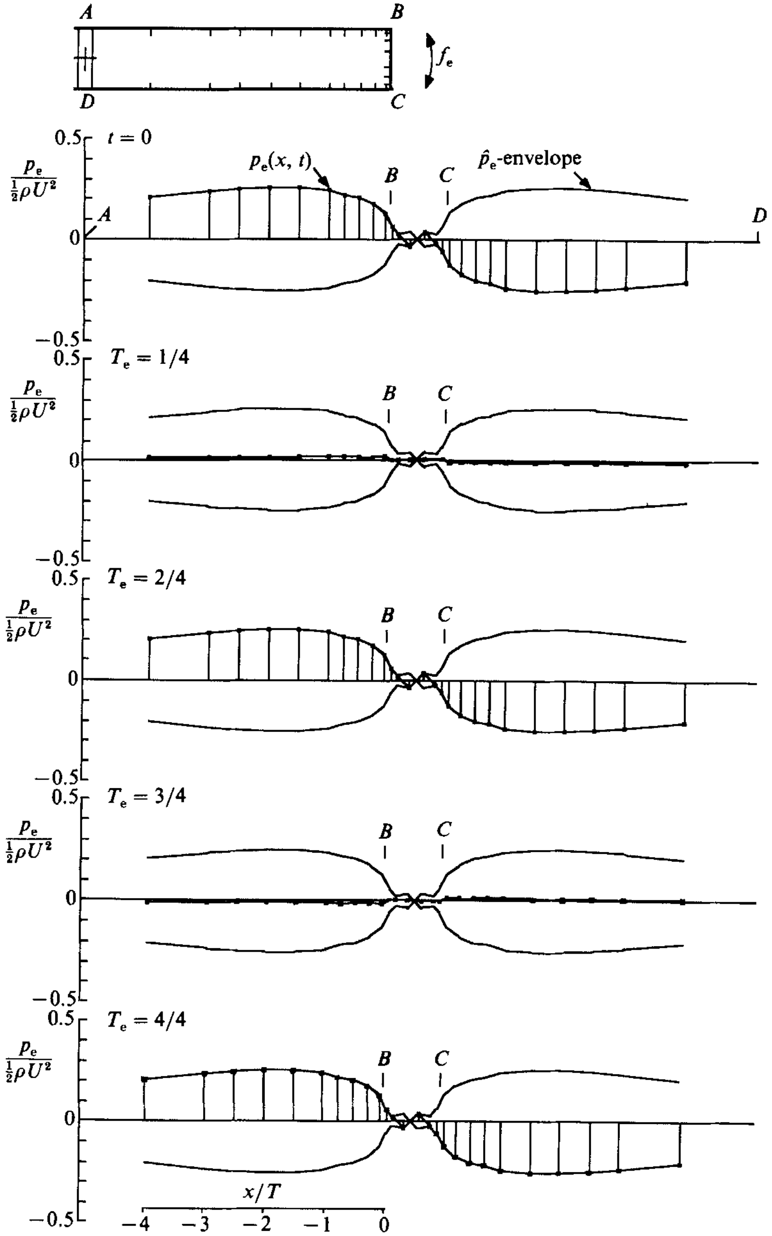

FIGURE 7. Time sequence of the instantaneous pressure field for oscillations in still water ($f_e = 2$ Hz, $\hat{\eta}_e = 0.02$).

phase. Therefore, the measured pressure fluctuations can be approximated as a superposition of the following two cosine components:

$$p(x,t) = p_0(x,t) + p_e(x,t)$$
$$= \hat{p}_0(x)\cos\{2\pi f_0 t + \phi_0(x)\} + \hat{p}_e(x)\cos\{2\pi f_e t + \phi_e(x)\}. \quad (4)$$

The phase $\phi_0(x)$ is the phase of the 'natural' vortex shedding; for practical reasons it is defined with respect to the most upstream pressure tap (see figure 3). The phase

$\phi_e(x)$ is the phase between the component of the local pressure fluctuations at f_e on the lower surface and the displacement signal $\eta(t)$ defined by (2). The frequency f_0 of the self-excited vortex shedding generally is influenced by the external excitation and is not identical to the frequency f_0^* of 'natural' vortex shedding in the absence of edge oscillation. The frequency $f_0^* = 1.95$ Hz will be employed for normalization in the following.

5.2. *Representative pressure variations*

Before describing the response functions of all pressure components in the form of three-dimensional plots, it is helpful to point out some of the basic characteristics of the induced pressures. In doing so, we consider the pressure responses at two extreme locations on the surface of the edge: one near the corner of the trailing edge (tap 10); and the other well upstream of it, at a distance of three trailing-edge thicknesses, $x/T = -3$ from the corner (tap 2). These measurements are displayed in figure 8.

Figure 8(*a*) shows the amplitude $\hat{p}_e$ of the pressure component at the excitation frequency f_e as a function of the normalized frequency f_e/f_0^*. The amplitudes $\hat{p}_e$ show distinct resonant behaviour for frequency ratios f_e/f_0^* close to 1; this resonance is marked near the corner of the trailing end, tap 10, while well upstream of it, tap 2, it is barely detectable. Furthermore, at sufficiently high excitation frequencies the non-circulatory or 'added mass' contributions dominate for both tap positions, evidenced by the fact that the data approach the curves of the measurements taken in still fluid.

The resonance of the pressure component $\hat{p}_e$ is accompanied by a jump in the phase angle ϕ_e between the pressure component $p_e(t)$ and the edge displacement $\eta(t)$, displayed in figure 8(*b*). Near the corner, at tap 10, this phase difference is characterized by a value of approximately π. On the other hand, well upstream of the end, at tap 2, the phase jump has an amplitude of nearly 2π. As will be evident in subsequent three-dimensional plots, this change from π to 2π phase difference occurs gradually in the streamwise direction.

Figure 8(*c*) shows the response of the pressure component $\hat{p}_0$, i.e. that component at the self-excited vortex formation frequency f_0, in the presence of forced oscillations of the edge. At tap 2, located well upstream of the trailing end, the pressure component $\hat{p}_0$ becomes very small and no frequency-dependent effects are discernable; this is not so for tap 10 close to the corner, where the pressure induced by the self-sustained vortex shedding is maximum (compare with figure 3). We note that irrespective of the excitation frequency f_e, there is always a spectral component at f_0. For sufficiently low frequency ratios, $f_e/f_0^* < 0.7$, the frequency f_0 of the pressure component $\hat{p}_0$ is relatively uninfluenced by the excitation. In this same frequency range, the amplitude of the pressure $\hat{p}_0$ also is little affected by the excitation. However, over the frequency range where $\hat{p}_e$ shows resonance, $0.9 < f_e/f_0^* < 1.1$, the pressure amplitude $\hat{p}_0$ is strongly attenuated and, over a narrow range, seems to vanish. Furthermore, within this resonance range occurs the largest influence on the frequency f_0 of the self-sustained vortex shedding. Below resonance, the frequency f_0 increases by a maximum of 15% and above resonance there is a maximum decrease in frequency of about 15%. We note that the data do not asymptotically approach the line $f_e = f_0$; instead, there is an abrupt jump at the resonance of the $\hat{p}_e$ component. Finally, we note two additional trends of the self-excited component due to the excitation at high frequency. Above resonance, the ratio f_e/f_0^* is always lower than unity, and for $f_e/f_0^* > 2.5$ the frequency f_0 of the self-sustained vortex shedding 'locks-on' to the $f_e = 3f_0$ characteristic. We expect corresponding alterations of the near-wake structure.

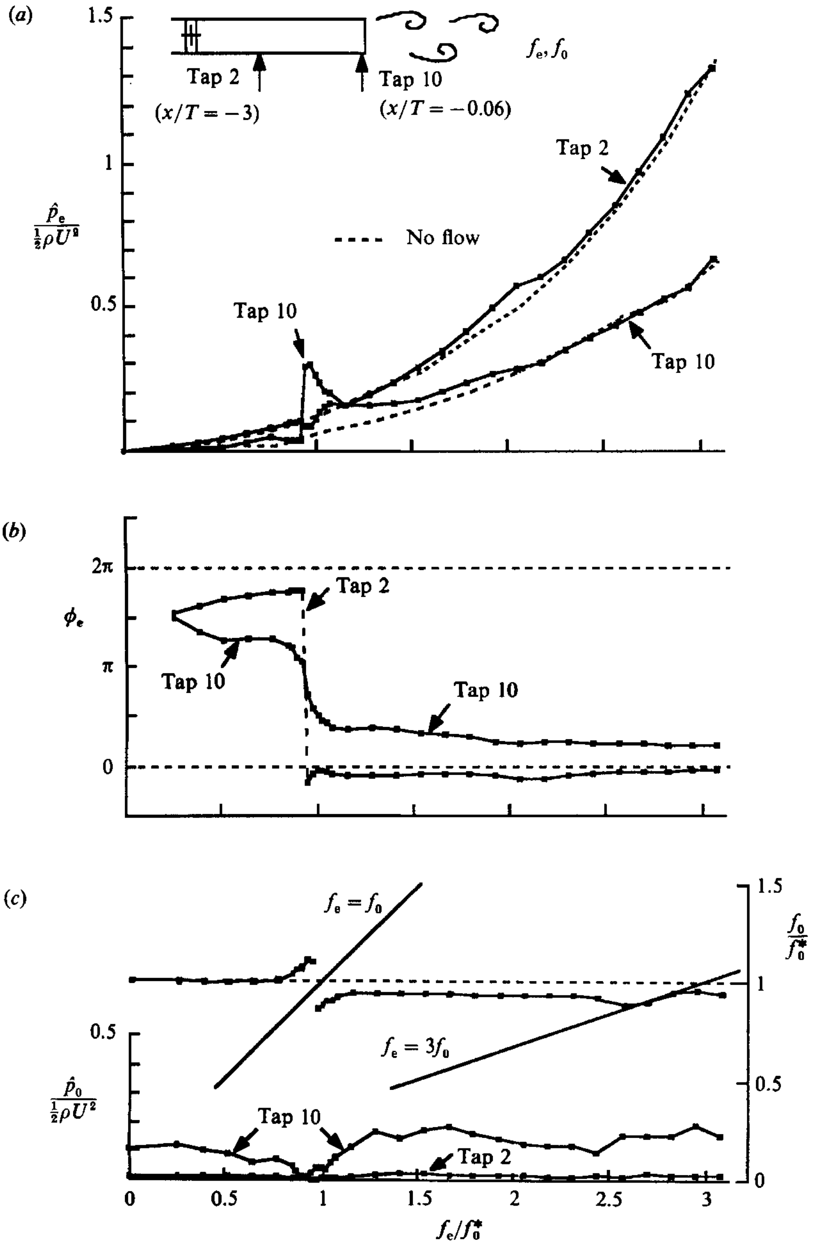

FIGURE 8. Typical response characteristics of the pressure fluctuations due to interaction of vortex shedding and edge oscillation at amplitude $\bar{\eta}_e = 0.02$ showing: (*a*) amplitude of pressure fluctuations $\hat{p}_e$; (*b*) phase angle ϕ_e between the pressure fluctuations $p_e(t)$ and the edge displacement $\eta_e(t)$; and (*c*) amplitude $\hat{p}_0$ of the self-sustained pressure fluctuations and the associated frequency f_0 of the self-sustained vortex shedding.

5.3. *Three-dimensional overviews*

Three-dimensional plots of the measured response functions of the spectral components at f_e and f_0 are given in figures 9–12. Pressure measurements were acquired along the midplane *A–B–C–D* of the trailing edge for a range of excitation f_e/f_0^*. The scales of figures 9–12 were chosen to be identical with figure 5, allowing direct comparison of the results; the only difference is that pressure and frequency are given now in dimensionless form. Again, the vertical trailing end, *C–B*, is projected onto the horizontal axis as a continuation of the lower surface *D–C*. The axis of rotation of the oscillating trailing edge is located between *A* and *D* (see figures 2 and 3).

Considering figures 9(*a*) and 9(*b*), for different oscillation amplitudes, we observe generally the same shape of the pressure distributions of $\hat{p}_e$ as for edge oscillations in still water (see figure 5) with the important difference that there is now a distinct, local resonance peak in the corner region for f_e/f_0^* close to 1. Within this resonance range the pressure amplitudes reach values that exceed those of oscillations in still water by a factor of 5. Furthermore, these local pressure fluctuations are a factor of 3 larger than those induced by the natural vortex shedding in absence of edge oscillations. It is interesting to note that, for all excitation frequencies, the pressure component $\hat{p}_e$ tends to the same peak value for the taps close to the corner on the lower (horizontal) and end (vertical) surfaces. The resonant values of $\hat{p}_e$ increase if we double the amplitude of oscillation from $\hat{\eta}_e = 0.01$ to 0.02 but they do not increase linearly with amplitude as the 'added mass' contributions do (compare figure 5). In summary, these resonant characteristics of the $\hat{p}_e$ component are clearly due to the shedding of vorticity in harmony with the motion of the edge. It is this circulatory contribution that dominates the pressure fluctuations in the trailing-end region near $f_e/f_0^* = 1$. On the other hand, at higher values of f_e/f_0^*, there is no longer synchronization of the vortex shedding and the non-circulatory (vertical mass) contribution prevails.

The phase $\phi_e(x)$ between the pressure fluctuations $p_e(x, t)$ on the lower surface and the displacement signal $\eta(t)$ is displayed in figure 10. The three-dimensional distributions of figure 10(*a*) and 10(*b*) resemble each other and show the same characteristic phase jump for excitation frequencies in the vicinity of $f_e/f_0^* = 1$. For the higher displacement amplitude of figure 10(*b*), the phase jump of 2π occurs closer to the corner of the edge; the corner is located at *C*. Irrespective of the value of x/T, there is an abrupt change in phase parallel to the f_e/f_0^* axis; it always occurs in the vicinity of $f_e/f_0^* = 1$. Remarkable is the fact that the magnitude of this phase 'jump' decreases substantially as the corner (*C*) of the edge is approached. It has an asymptotic value $\Delta\phi_e = 2\pi$ upstream of the corner and decreases to $\Delta\phi_e \approx \frac{1}{2}\pi$ at the base of trailing end. Moreover, the magnitude of this phase jump goes to its minimum value as the midline of the (vertical) base surface *C–B* is approached. In other words the entire pressure field along the surface of the trailing edge undergoes a phase jump $\Delta\phi_e$ simultaneously within a small interval of excitation frequency near $f_e/f_0^* = 1$, even though the magnitude of the jump varies with location. Furthermore, at a given value of f_e/f_0^*, it is evident that the phase gradient $\mathrm{d}\phi_e/\mathrm{d}x$ has a different sign before and after the jump. Below resonance, ϕ_e decreases in the direction of flow, while above resonance it increases. The existence of an absolute instability in the near wake (Monkewitz & Nguyen 1987), which admits upstream wave motion, may be related to this observation. Further theoretical studies are necessary to establish whether the opposite phase gradients upstream of the corner of the edge, occurring for $f_e/f_0^* > 1$ and $f_e/f_0^* < 1$, are related to different directions of wave propagation along the surfaces of the trailing edge. However, we can conclusively state, and wish to underscore that, as excitation passes through the range $f_e/f_0^* \approx 1$, not only does the initially shed vortex switch from one corner of the trailing edge to the other, but there is a switch in sign of the phase gradient of the trailing-edge pressure field. Irrespective of the possible interpretations of this observation in terms of convective

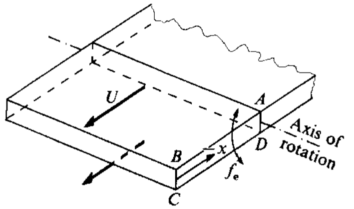

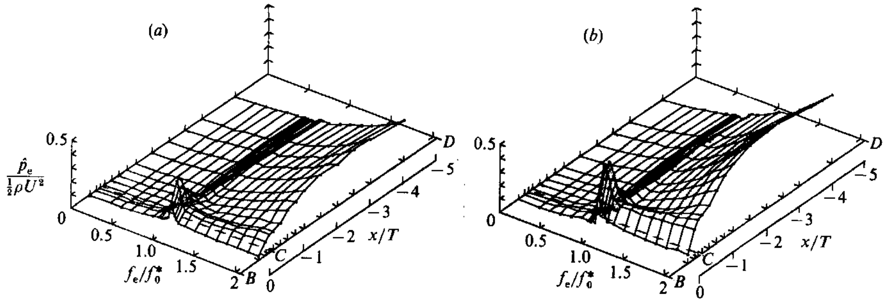

FIGURE 9. Amplitude $\hat{p}_e$ of the pressure fluctuations at the frequency f_e of the edge oscillation showing: (*a*) oscillation at amplitude $\hat{\eta}_e = 0.01$; and (*b*) at $\hat{\eta}_e = 0.02$.

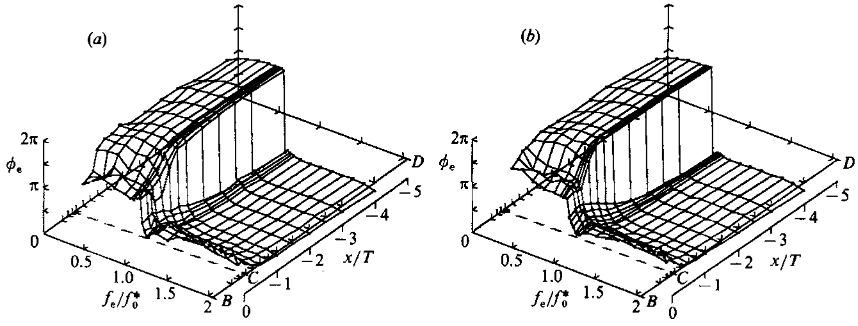

FIGURE 10. Phase angle ϕ_e between the pressure fluctuations $p_e(t)$ and the edge displacement $\eta_e(t)$ showing: (*a*) oscillation at amplitude $\hat{\eta}_e = 0.01$; and (*b*) at $\hat{\eta}_e = 0.02$.

or absolute instabilities in the near-wake region, the change in sign of the streamwise phase gradient does indicate a drastic alteration in character of the surface pressure wave in the trailing-edge region.

Figures 11 and 12 show the pressure component $\hat{p}_0$ of the self-sustained vortex shedding at f_0 in the presence of edge oscillations at f_e. We clearly see in figure 11 that pronounced pressure fluctuations induced by the self-sustained vortex shedding occur only in a limited region upstream of the corner *C* and on the vertical base *C–B*. At excitation frequencies f_e/f_0^* away from $f_e/f_0^* = 1$, the streamwise distributions of $\hat{p}_0$ agree with those of the stationary edge (compare with figure 3). Furthermore, we observe that there is a range of marked attenuation of $\hat{p}_0$ for excitation frequencies near $f_e/f_0^* = 1$, i.e. in the range of resonant response of $\hat{p}_e$. This attenuation, or quenching, of $\hat{p}_0$ occurs along the entire streamwise extent of the trailing edge, indicating that either the self-sustained flow oscillation is actually attenuated or that the corresponding vortex formation is shifted further downstream from the trailing end. Either of these phenomena would reduce the magnitude of the pressure. If we characterize this quenching of $\hat{p}_0$ in terms of typical response of a nonlinear oscillator,

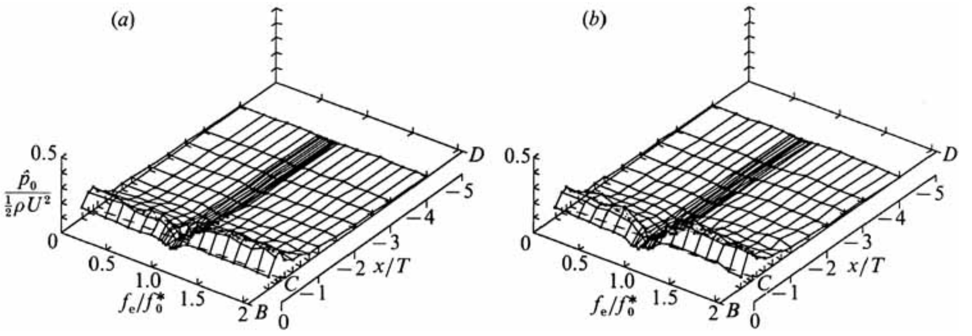

FIGURE 11. Amplitude $\hat{p}_0$ of the pressure fluctuations at the frequency f_0 of the self-sustained vortex shedding showing: (a) oscillation at amplitude $\hat{\eta}_e = 0.01$; and (b) at $\hat{\eta}_e = 0.02$.

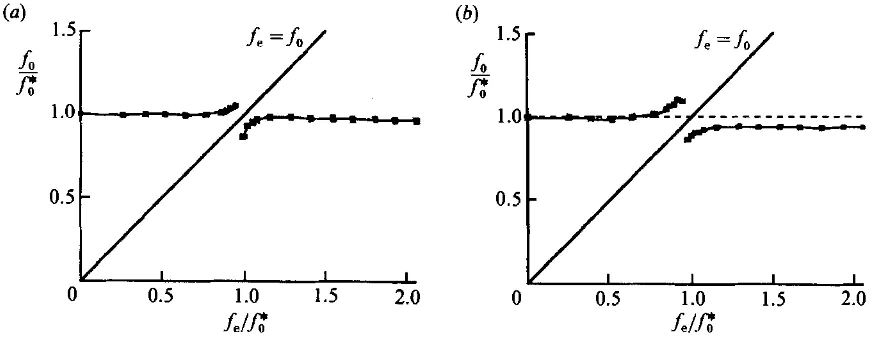

FIGURE 12. Frequency f_0 of the self-sustained pressure fluctuations $\hat{p}_0$ showing: (a) oscillation at amplitude $\hat{\eta}_e = 0.01$; and (b) at $\hat{\eta}_e = 0.02$.

we can classify it as 'asynchronous quenching'; this and related aspects are discussed in detail by Staubli (1987) for a variety of flow oscillations.

Simultaneously with this attenuation of $\hat{p}_0$, we observe a shift of the frequency f_0 away from the excitation frequency f_e, as indicated in figure 12. In other words the timescale $T_0 = 1/f_0$ of the self-sustained vortex formation process is substantially altered as the limit $f_e/f_0^* = 1$ is approached.

6. Instantaneous pressure field and flow structure

6.1. Regimes

Over the range of excitation frequency, we can classify several regimes of the flow structure and the associated pressure distributions. At *subresonant excitation*, with $f_e \ll f_0^*$, the structure of the self-sustained, 'natural' vortex shedding dominates the flow field. The controlled oscillation of the edge modulates, in a weak fashion, the self-sustained vortex formation. This modulation is detected at the difference of the two frequencies $f_e - f_0$. A special case of this subresonant excitation is *subharmonic excitation*, i.e. $f_e = \frac{1}{2}f_0$, where the flow pattern repeats after each half-cycle of external excitation.

The next regimes are *preresonant excitation* and *resonant excitation*. Here, the flow field is dominated by vortex shedding at the excitation frequency f_e and appears, to a first approximation, as periodic at f_e. Pressure measurements indicate strongly attenuated fluctuations at the frequency f_0 of the self-sustained vortex shedding. These regimes are distinguished into preresonant and resonant because $\hat{p}_e$ shows, for preresonance, no enhanced amplitude; on the other hand, for resonance, the amplitudes of $\hat{p}_e$ are strongly amplified (compare figure 8). In the transition from preresonant to resonant excitation, the formation region of the vortices in the near wake undergoes significant changes; furthermore, the phasing of the initially formed vortex shifts dramatically relative to the displacement of the trailing edge. This observed change in the flow structure agrees with the phase jump observed for the pressure fluctuations within this frequency range. An overview on these changes in flow structure and pressure will be given in figure 17.

Finally, a fourth regime can be characterized as *excitation above resonance*. In this regime, with $f_e > f_0^*$, the structure of the externally excited vortex formation dominates the flow field immediately behind the trailing end. A little further downstream, the flow structure of the self-sustained vortex formation emerges from interaction of the small-scale vortices due to excitation. A special case of excitation above resonance is *superharmonic excitation*, i.e. $f_e = 2f_0$, where the flow pattern repeats after every second cycle of external excitation; at the superharmonic excitation $f_e = 3f_0$, there is a 'lock-on' effect.

In the following, these regimes are discussed in detail.

Subresonant excitation

Figure 13 shows an example of a time sequence of the visualized flow structure in conjunction with the instantaneous pressure fields and forces for subresonant excitation, or more precisely, for the special case of subharmonic excitation. In the upper left corner of each schematic, the rotating phasors of edge displacement $\hat{\eta}_e$ and the resultant force $\hat{F}_e$ are depicted; they rotate counterclockwise with increasing time. The angle between them remains fixed; it represents the lag of the force $F_e(t)$ with respect to the displacement $\eta(t)$. Also indicated in figure 13 are the amplitude envelopes of the pressure fluctuations $\hat{p}_e(x)$ upon the surface; they represent the extreme values of the pressure fluctuations during a cycle of oscillation. The magnitude of the instantaneous pressure $p_e(x, t)$ is indicated by the vertical lines. The dashed line indicates the amplitude envelope of the pressure component $\hat{p}_0(x)$ due to the self-sustained vortex shedding. Within the schematic of the trailing edge, there is representation of the envelopes of the two force components $F_e(t)$ and $F_0(t)$. The extremes of these envelopes go to ± infinity; they are truncated here. Moreover, the instantaneous amplitude of force $F_e(t)$ at its instantaneous position is shown in the form of a bold, vertical bar.

The time interval between each of these composites of flow structure, pressure and force corresponds to one quarter of the period $T_e = 1/f_e$ of the external excitation, as described in the figure caption. The first and fifth photos show the trailing edge at its maximum positive displacement. Since, for this example, the period of the self-sustained vortex shedding is half the period of the edge oscillation, i.e. $T_0 = \frac{1}{2}T_e$, the photo sequence depicts two cycles of self-sustained vortex shedding. This, and the fact that the external excitation has little effect on the self-sustained vortex shedding, explain the repetition of the flow structure in the photo series. The photo in the middle, taken at $t/T_e = \frac{1}{2}$, resembles closely the first and the last photos taken at the same phase in the edge oscillation cycle. The fact that the flow structure at f_0 dominates the wake is further reflected in the envelopes of the pressure fluctuations

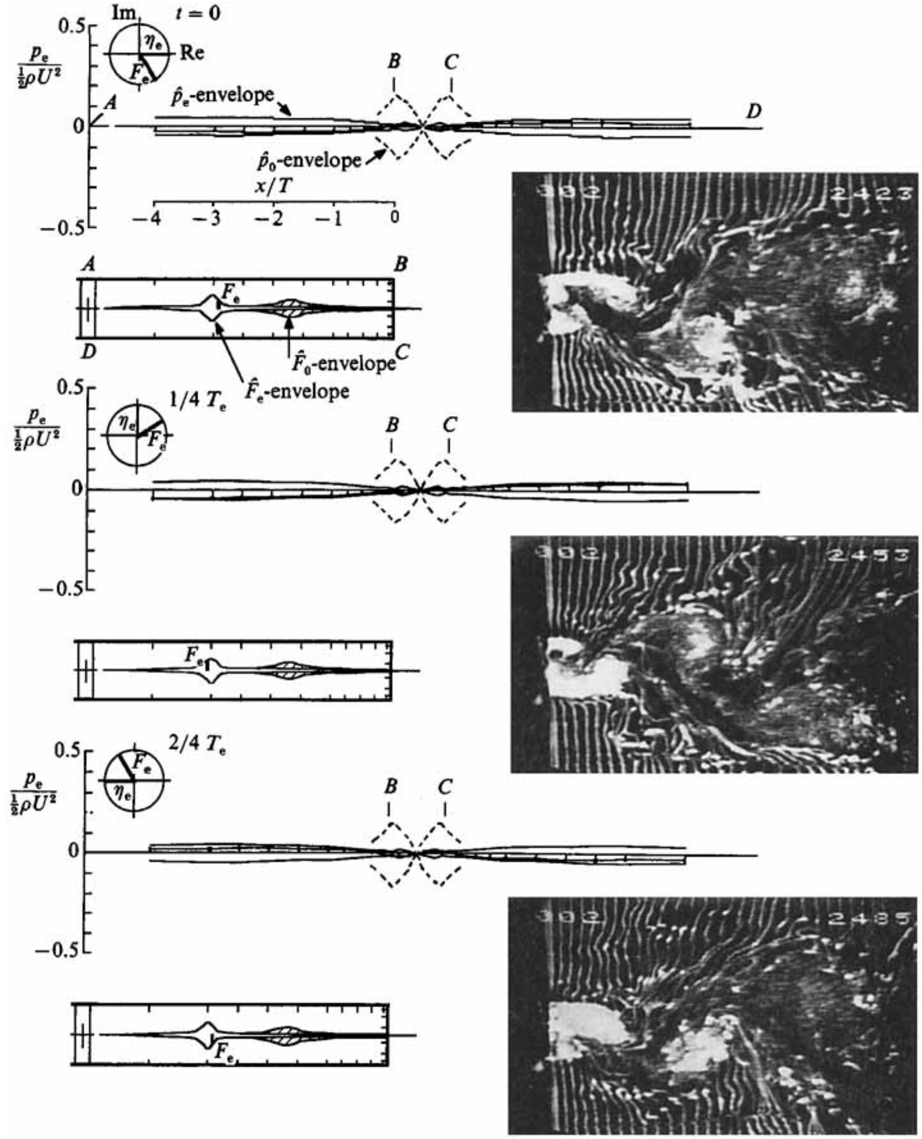

FIGURE 13. For caption see facing page.

$\hat{p}_e$ and $\hat{p}_0$. Whereas the pressure fluctuation $\hat{p}_0$ exhibits a large amplitude in the region of the corners at B and C (compare with figure 4), the component $\hat{P}_e$ is barely detectable there.

Concerning the resultant forces $F_0(t)$ and $F_e(t)$, their amplitudes are of the same order; the maximum of the force envelope $\hat{F}_e$ is located well upstream of the trailing end. (We note that in integrating the pressure distribution $p_e(x, t)$, the pressure distribution was extrapolated towards the axis of rotation.)

Preresonant excitation

In figure 14 the case of excitation at $f_e/f_0^* = 0.87$ is depicted. At this frequency the self-sustained pressure fluctuations $\hat{p}_0$ are attenuated (see figure 8c); moreover, the

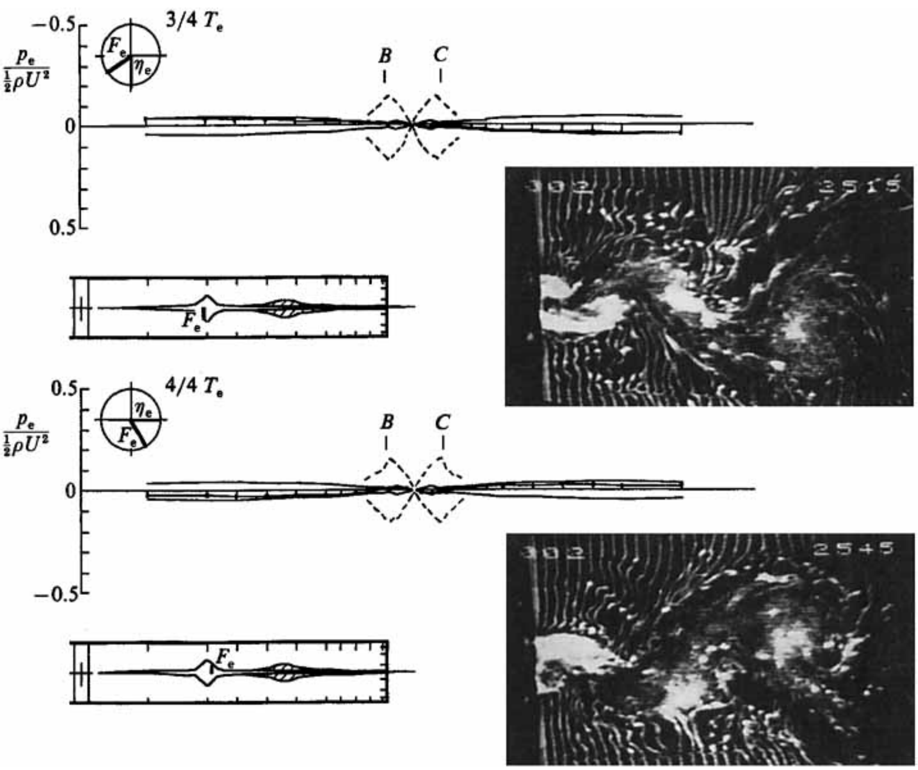

FIGURE 13. Time sequence of the flow structure and the corresponding instantaneous pressure field for one cycle of subharmonic edge oscillation at $f_e/f_0^* = 0.5$ and $\hat{\eta}_e = 0.02$ ($t = 0$; $t/T_e = 1/4$; $t/T_e = 1/2$; $t/T_e = 3/4$; $r/T_e = 1$).

component $\hat{p}_e$ does not yet undergo resonant amplification. This frequency of excitation lies just below the onset of the phase jump (see figure 8*b*). This sequence of photographs suggests that the vortex cores are elongated and not as distinct as at lower (figure 13) or higher (figure 15) excitation frequency. Moreover, the distance to formation of a distinct vortex seems to have increased relative to the lower frequency of figure 13.

Regarding the phasing of vortex formation from the corners of the trailing end relative to the edge displacement, the top photo shows that when the edge is at its highest (maximum positive) position, i.e. $\eta(t) = +\hat{\eta}_e$, the vortex near the lower corner starts forming. After a half-cycle, the converse occurs and the upper vortex is in the process of forming. Finally, with minor modulation, the flow pattern repeats after completion of the full cycle when the edge is again at its highest position. Because of the mirror image of the flow patterns at $t/T_e = \frac{1}{2}$ with respect to those at $t/T_e = 0$ and $t/T_e = 1$, we conclude that the flow structure induced by the excitation frequency f_e dominates the flow field.

There are further interesting features of the instantaneous pressure distributions of figure 14. In the distribution at $t/T_e = 0$, we see that pressure fluctuations $p_e(x, t)$ upstream of the corners are dominated by non-circulatory or 'added mass' effects; this observation follows from the fact that the instantaneous pressure distributions have the shapes of those observed in the case of oscillations in still water (see figure 7); moreover, on the upper surface, the pressure is more or less in antiphase relative

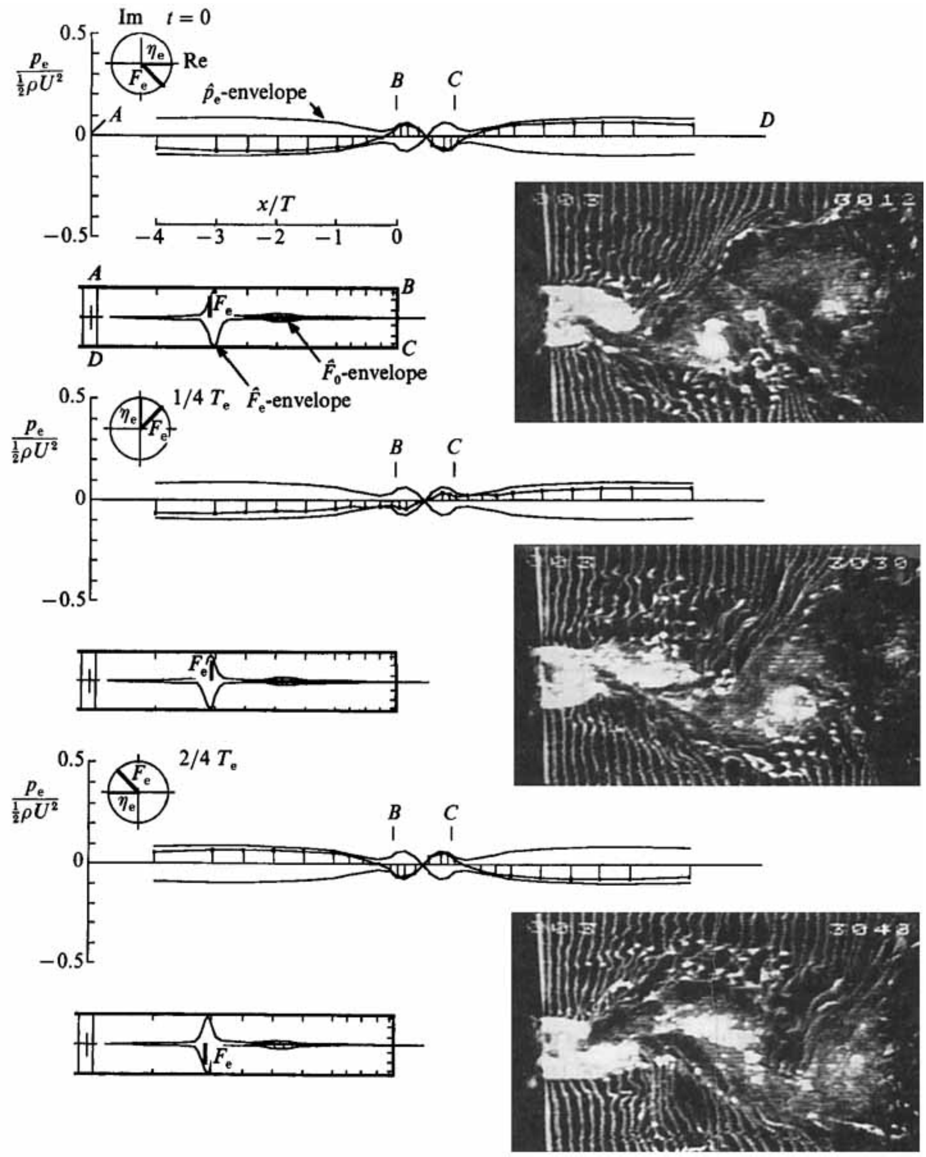

FIGURE 14. For caption see facing page.

to the displacement and, accordingly, on the lower surface they are in-phase with $\eta(t)$. Considering pressure fluctuations in the corner and base regions, we see that they ocur out-of-phase with the respective fluctuations along the upstream surfaces. In other words, pressures induced by vortex shedding at f_e are out-of-phase with 'added mass' effects, a fact which already could have been concluded from the information that vortex formation starts on the lower side when the edge is in the highest position. This phasing, as mentioned before, is an important feature of the transition from preresonance to resonance and also to excitation above resonance.

The instantaneous force $F_e(t)$, shown within the phase circle, lags the edge displacement $\eta(t)$, as was the case for subresonant excitation. In contrast to the

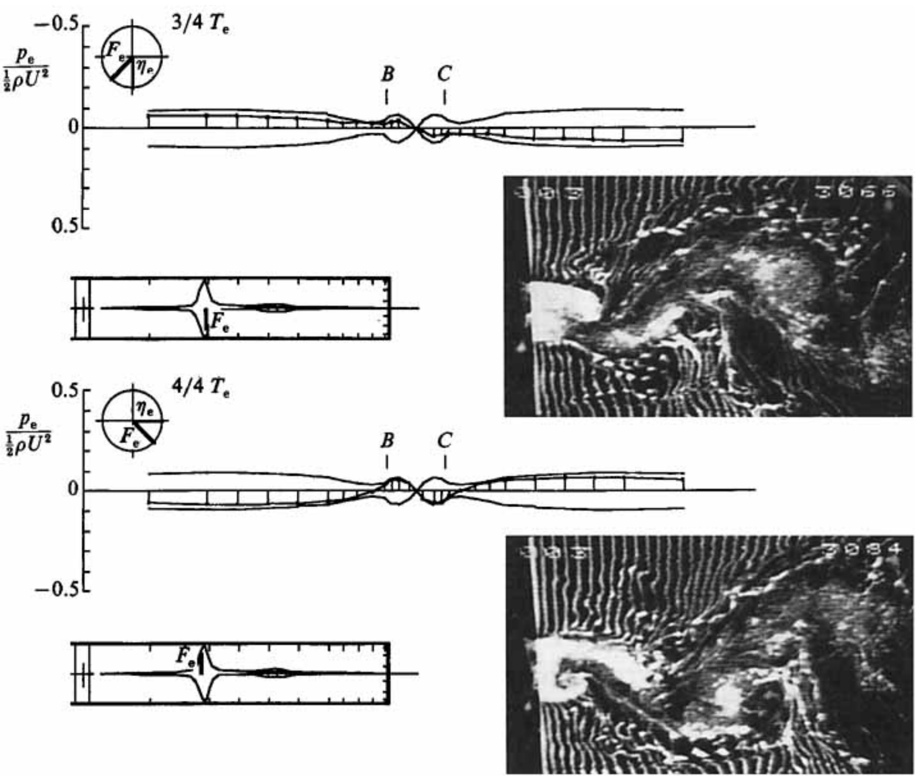

FIGURE 14. Time sequence of the flow structure and the corresponding instantaneous pressure field for preresonant edge oscillation at $f_e/f_0^* = 0.87$ and $\hat{\eta}_e = 0.02$ ($t = 0$; $t/T_e = 1/4$; $t/T_e = 1/2$; $t/T_e = 3/4$; $t/T_e = 1$).

subresonant example of figure 13, the maximum force amplitude of $\hat{F}_e$ now dominates that of $\hat{F}_0$ arising from the self-sustained vortex shedding.

Resonant excitation

Comparison of the flow structure with that of previous series indicates that the large-scale vortex formation at $f_e/f_0^* = 1.02$ shown in figure 15 is now much more coherent; the vortical structures appear to be more concentrated, indicated by bright regions of bubbles in their centres. Regarding the phasing of the vortex formation from the corners, we observe from the instantaneous pressure distribution $p_e(t)$, as well as from visualization, that the lower vortex now starts forming at $t/T_e = \frac{1}{4}$. At this instant we have maximum negative velocity of the trailing end, and simultaneously, maximum negative pressure near the lower corner. Comparing with the preresonant case of figure 14, we see that the formation of the vortex from the lower corner in figure 15 (at $t/T_e = \frac{1}{4}$) now lags that of figure 14 (at $t/T_e = \frac{1}{2}$) by the order of $\frac{1}{2}\pi$; this observation is confirmed by the phase distribution in figure 8(*b*), tap 10, and in figure 10 in the corner region. Upstream of the corner region we note that the amplitude and phase distributions of the pressure now follow perfectly those of the 'added mass', i.e. edge-induced, distributions given in figure 7. Vortex-induced pressures in the corner regions lead the 'added mass', pressures by $\frac{1}{2}\pi$.

The phase of the resultant force component $F_e(t)$, as depicted in the phase clock,

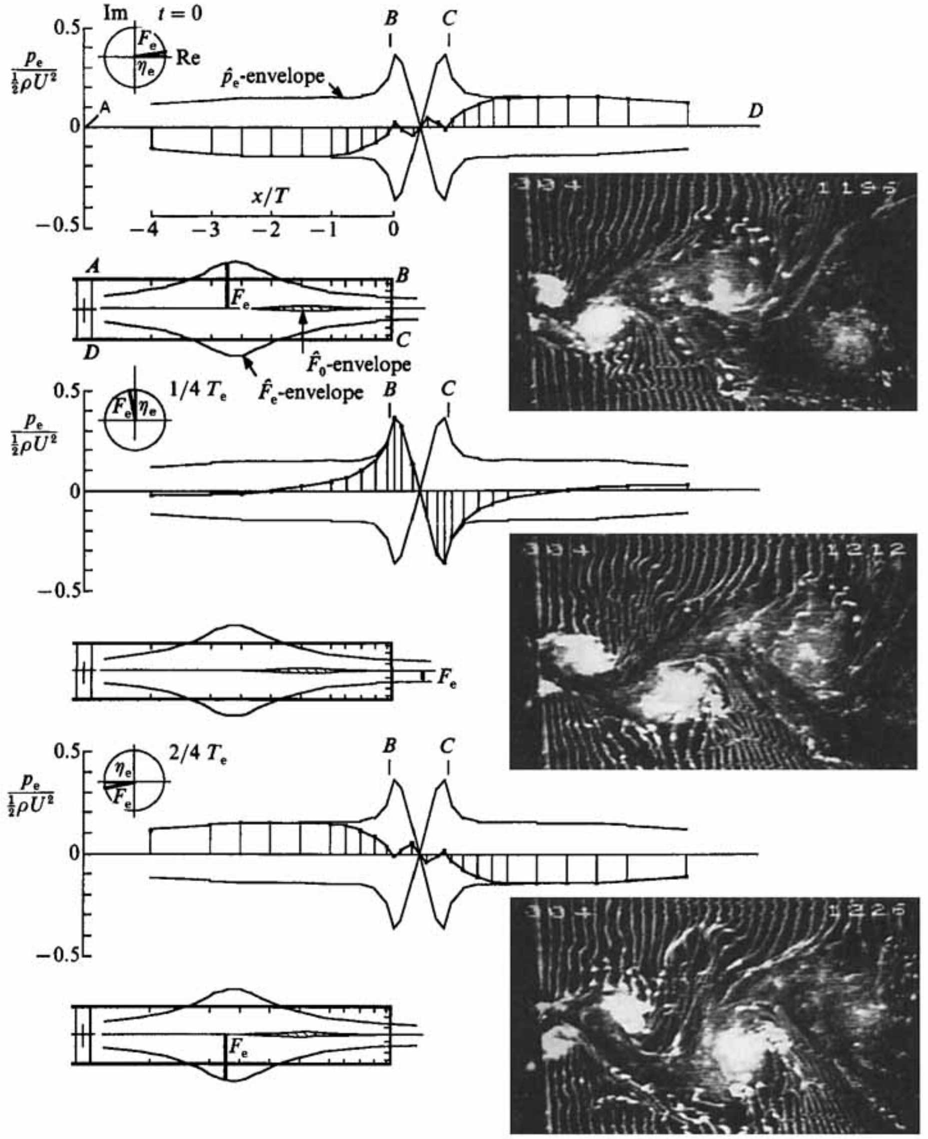

FIGURE 15. For caption see facing page.

lags that of the preresonant regime by approximately $\frac{3}{2}\pi$. (That it is a lag of $+\frac{3}{2}\pi$ and not a lead of $\frac{1}{2}\pi$ will be demonstrated in the next section.) In absolute terms, $F_e(t)$ now leads the displacement $\eta(t)$, in contrast to the preresonant regime (figure 14), where it substantially lagged $\eta(t)$. This phase shift is in accord with the phase distributions of figure 10 and the phasing of the visualized vortex formation described in the foregoing. Therefore, the force magnitude $\hat{F}_e$ completely dominates $\hat{F}_0$ due to the nearly complete quenching of the pressure component $\hat{p}_0$ (see figure 11*b*) and the enhanced vortex formation at f_e which induces larger (resonant) pressure amplitudes $\hat{p}_e$ (see figure 9). Concerning the force component $\hat{F}_e$, it undergoes substantial streamwise excursions. As will be discussed subsequently, the point of application of $\hat{F}_e$ can be located downstream of the trailing edge or upstream of the flexible joint due to the phase difference of the integrated force and torque fluctuations.

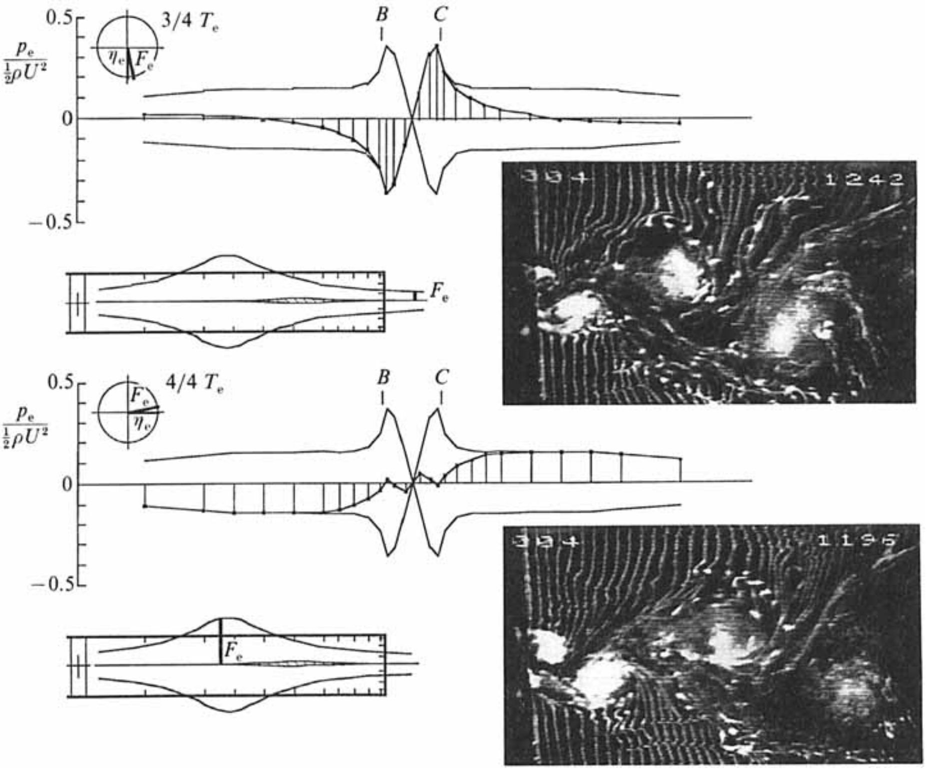

FIGURE 15. Time sequence of the flow structure and the corresponding instantaneous pressure field for resonant edge oscillation at $f_e/f_0^* = 1.02$ and $\hat{\eta}_e = 0.02$ ($t = 0$; $t/T_e = 1/4$; $t/T_e = 1/2$; $t/T_e = 3/4$; $t/T_e = 1$).

Excitation above resonance

At the excitation frequency $f_e = 2f_0^*$, depicted in figure 16, the instantaneous pressure distribution $p_e(t)$ clearly is dominated by the non-circulatory, or 'added mass', effects and so is the force component $\hat{F}_e$. The envelope of the force component $\hat{F}_0$ now takes on the same amplitude and shape as observed for the 'natural' vortex shedding in the absence of edge oscillations (see figure 4).

Vortex-induced pressures $\hat{p}_e$ near the trailing end reach maximum amplitudes for $t/T_e = \frac{1}{4}$ and $t/T_e = \frac{3}{4}$ since instantaneous values coincide at these instants with the envelopes of $\hat{p}_e$. In contrast, 'added mass'-induced pressures in the upstream region of the edge approximately follow the envelopes of $\hat{p}_e$ for $t = 0$, $t/T_e = \frac{1}{2}$ and $t/T_e = \frac{4}{4}$. Therefore, as in the case of resonant excitation described in the preceding section, vortex-induced pressures near the trailing end lead 'added mass'-induced pressures in the upstream region of the edge by $\approx\frac{1}{2}\pi$.

The edge oscillation dominates the flow field immediately behind the trailing end, where there is small-scale vortex formation at frequency f_e. However, the vortices at about one or two trailing-edge thicknesses downstream from the trailing end are recovered vortices of the self-sustained flow oscillation, i.e. of the 'natural' vortex shedding at f_0. This follows from the fact that the downstream vortices in the first and last photos show patterns that are mirror images, indicating that half a period of the large-scale vortex formation has elapsed. Knowing from pressure measure-

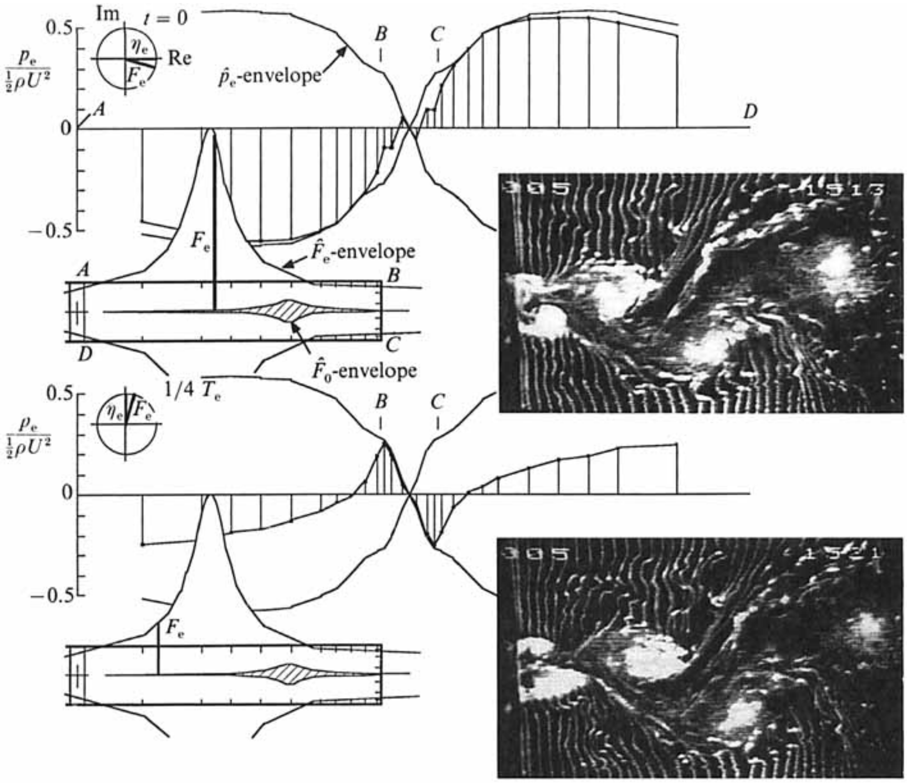

FIGURE 16. For caption see facing page.

ments that $T_0 = 2.19T_e$ in this regime, we can associate these vortices with the self-sustained vortex shedding. Furthermore, if we compare the wavelength of these vortices with the wavelength of the vortices shed in the absence of edge oscillations (see figure 4), we notice good agreement; vortices with the frequency $f_e = 2f_0^*$ would show approximately half this wavelength.

Overview of instantaneous pressure fields

Common features of, and distinctions between, the instantaneous pressure fields described in the foregoing are brought forth in figure 17, which shows excerpts from each of the basic regimes of excitation given in figures 4 and 14–16. The criterion for selecting each of the excerpts was occurrence of maximum instantaneous pressure gradient between the upper (B) and lower (C) corners of the trailing end.

Consideration of the amplitude envelopes of the $\hat{p}_0(x)$ component at $f_e/f_0^* = 0$ and of the $\hat{p}_e(x)$ component at $f_e/f_0^* = 0.87$ and 1.0 shows that they all have a similar form near the corners of the edge. Maximum pressure amplitudes occur at or near the corners B and C. As consequence, application of a Kutta condition with respect to the fluctuating pressures is indeed inappropriate for either the stationary or perturbed edge. The pressure amplitude does not go to zero (over a lengthscale commensurate with that of the edge length) as the corner of the edge is approached. Rather, it exhibits a rapidly increasing amplitude, irrespective of whether the corner is approached along the horizontal surface or along the vertical (base) surface.

At the midposition (midway between B and C) on the vertical face of the trailing end, the pressure envelopes $\hat{p}_0$ and $\hat{p}_e$ have zero magnitude for all values of f_e/f_0^*;

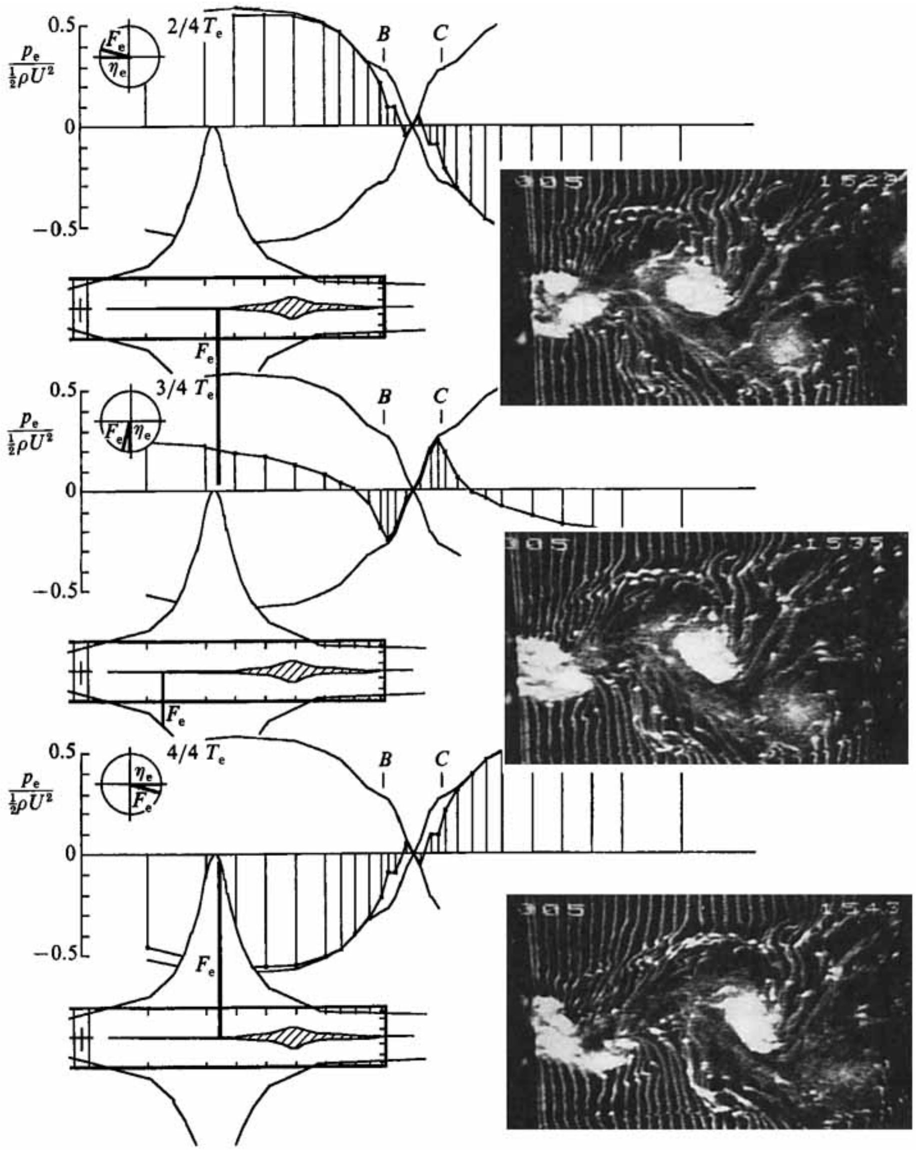

FIGURE 16. Time sequence of the flow structure and the corresponding instantaneous pressure field for edge oscillation at $f_e/f_0^* = 2.0$ and $\hat{\eta}_e = 0.02$ ($t = 0$; $t/T_e = 1/4$; $t/T_e = 1/2$; $t/T_e = 3/4$; $t/T_e = 1$).

consequently, at all instants during the oscillation cycle, the pressure amplitude remains at a zero value. For the two pressure taps close to the midposition, contributions due to the second harmonic ($2f_e, 2f_0$) components were of the same order of magnitude as the corresponding ones at the fundamental (f_e, f_0) components; at the midposition of the trailing end, contributions due to the second harmonic reach their maximum.

Upstream of the trailing end, all of the amplitude envelopes of the $\hat{p}_e(x)$ component show a region of nearly uniform amplitude. The corresponding instantaneous pressure distributions (see figures 10 and 14–16) exhibit negligible streamwise phase

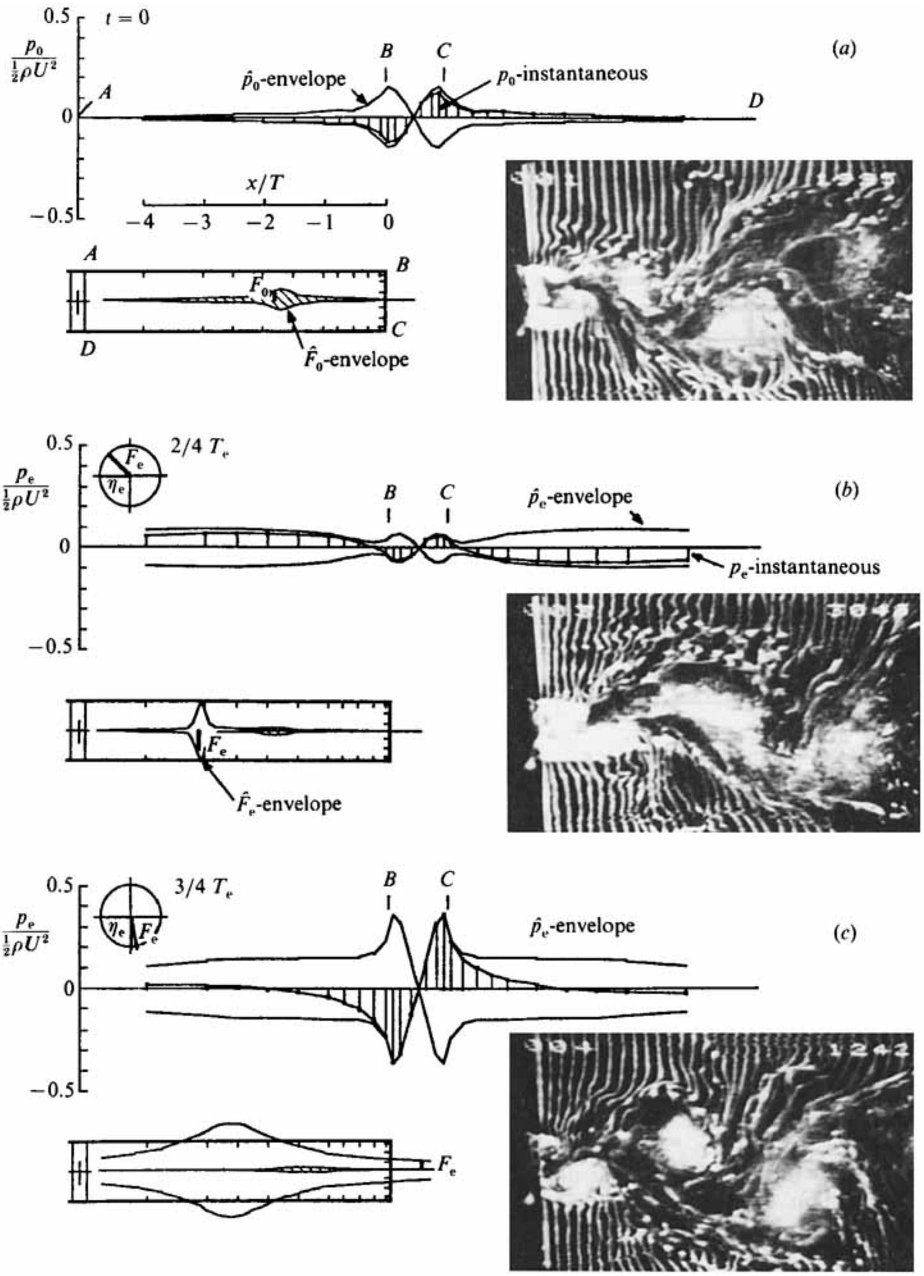

FIGURE 17. For caption see facing page.

variations. The pressure in these upstream regions is therefore due to the non-circulatory or 'added mass' contribution arising from the motion of the edge. Indeed, the amplitude of the pressure in this region goes as the square of f_e, as described in figures 5, 7 and 8. Moreover, we note that the amplitude of the circulatory or 'vortex-induced' contribution to the pressure exceeds that of the upstream non-circulatory value only in a region close to the corner and at an excitation frequency close to synchronization ($f_e/f_0^* \approx 1$) (see figure 17, $f_e/f_0^* = 1.02$ and figures 8 and 9).

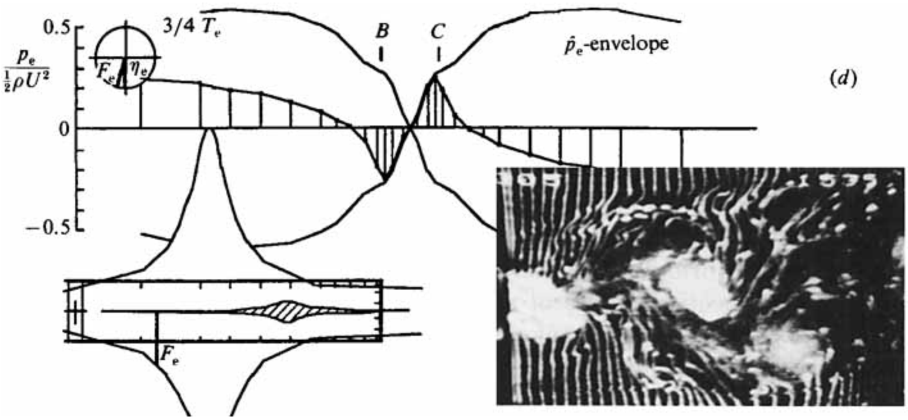

FIGURE 17. Comparison of instants of maximum vortex-induced pressures in the region of the trailing end showing: (*a*) the case of the non-oscillating trailing-edge, $f_e/f_0^* = 0$; (*b*) subresonant excitation, $f_e/f_0^* = 0.87$, edge in lower position; (*c*) resonant excitation, $f_e/f_0^* = 1.02$, edge in midposition; and (*d*) excitation above resonance, $f_e/f_0^* = 2.0$, edge in midposition.

By comparing the shapes of the instantaneous pressure distributions with those of the corresponding amplitude envelopes in figure 17, one obtains an indication of the phase shift of the instantaneous pressure (shown in detail in figures 3 and 10) along the surface of the edge. If, for example, the shapes of the pressure distributions are the same for all time, then the instantaneous pressure is in phase along the entire surface of the edge. At $f_e/f_0^* = 0$, the instantaneous pressure $p_0(t)$ is nearly in phase along the entire surface (compare figure 3), attributed entirely to the vortex shedding and the upstream influence of its near-wake pressure field. In the presence of excitation, i.e. $f_e/f_0^* \neq 0$, there exists a region of constant phase upstream of the corner of the edge. In this upstream region the pressure $p_e(t)$ is attributable to the motion of the edge, i.e. to non-circulatory or 'added mass' effects. For all excitation frequencies, there is substantial phase shift of the pressure $p_e(t)$ as the corner is approached, indicating increasing dominance of the circulatory or 'vortex-induced' pressure.

Now the resultant force $F_e(t)$ acting on the trailing edge will be due to both the non-circulatory and circulatory pressure contributions. As will be addressed, it is the phase shift of this force $F_e(t)$ with respect to the edge motion $\eta(t)$ that determines the direction of energy transfer between the surrounding fluid and the edge. We therefore are interested in determining which regions of the pressure field on the surface of the edge influence the phase shift of the force $F_e(t)$. No matter how large the non-circulatory contribution to the pressure $p_e(x,t)$ becomes with changes in f_e/f_0^*, its phase with respect to the edge displacement $\eta(t)$ remains, by definition, fixed at a value of π on the upper surface and at 0 or 2π on the lower surface (see figures 6 and 10). Therefore only the circulatory pressure $p_e(x,t)$ contribution (due to shedding of vorticity), whose phase with respect to $\eta(t)$ changes with f_e/f_0^*, can produce changes of the phase of $F_e(t)$ with respect to $\eta(t)$. Inspection of excerpts at $f_e/f_0^* = 0.87$ and 1.02 in figure 17, as well as the time series in figures 14 and 15, and the phase distributions of figure 10 all show that the circulatory contribution to the pressure is confined to a region less than one trailing-edge thickness T upstream of the corner; this distance corresponds to about one-half-wavelength λ_0 of the vortex formation (at frequency f_0) downstream of the edge. Therefore, only the region of the pressure field in the immediate vicinity of the corner determines the phase shift of $F_e(t)$ with respect to $\eta(t)$.

7. Force and point of application

7.1. *Definitions*

The consequence of the unsteady pressure field on the surface of the trailing edge is to produce forces at the excitation frequency f_e as well as at the frequency f_0 of the self-sustained vortex formation. In this section, we shall discuss the response of these forces and their respective points of application to the external excitation of the edge. As was done for the resultant pressure fluctuations in equation (4), we can approximate the force fluctuations in the time domain with the following superposition:

$$F(t) = F_0(t) + F_e(t) = \hat{F}_0 \cos 2\pi f_0 t + \hat{F}_e \cos \{2\pi f_e t + \phi_F\}. \tag{5}$$

The phase ϕ_F is the phase between the force component $F_e(t)$ and the displacement signal $\eta(t)$; for the force component $F_0(t)$ no such phase is defined.

The force component $F_e(t)$ results from integration of the instantaneous pressure distribution $p_e(x,t)$ along the surface of the trailing edge and, correspondingly, $F_0(t)$ results from integration of $p_0(x,t)$. The sign is defined such that a force in the positive η-direction has a positive value.

$$F_0(t) = \int_D^C p_0(\xi,t)\,\mathrm{d}\xi - \int_A^B p_0(x,t)\,\mathrm{d}\xi, \tag{6}$$

$$F_e(t) = \int_D^C p_e(\xi,t)\,\mathrm{d}\xi - \int_A^B p_e(\xi,t)\,\mathrm{d}\xi, \tag{7}$$

where $\xi = x + 5T$ and ξ is zero at the upstream end of the trailing edge at the flexible joint.

The instantaneous points of application $\xi_0(t)$ and $\xi_e(t)$ of the two force components at the frequencies f_0 and f_e result from division of the instantaneous torque by the instantaneous force and can be written as follows:

$$\xi_0(t) = \frac{\int_D^C \xi p_0(\xi,t)\,\mathrm{d}\xi - \int_A^B \xi p_0(\xi,t)\,\mathrm{d}\xi}{\int_D^C p_0(\xi,t)\,\mathrm{d}\xi - \int_A^B p_0(\xi,t)\,\mathrm{d}\xi}, \tag{8}$$

$$\xi_e(t) = \frac{\int_D^C \xi p_e(\xi,t)\,\mathrm{d}\xi - \int_A^B \xi p_e(\xi,t)\,\mathrm{d}\xi}{\int_D^C p_e(\xi,t)\,\mathrm{d}\xi - \int_A^B p_e(\xi,t)\,\mathrm{d}\xi}. \tag{9}$$

If we transform back to the original coordinate $x = \xi - 5T$ and introduce for the pressures $p_e(x,t)$ and $p_0(x,t)$ the sinusoidal fluctuations according to (4), then the two points of application take the following form:

$$x_0(t) = \bar{x}_0 + \hat{x}_0 \cot\{4\pi f_0 t\}, \tag{10}$$

$$x_e(t) = \bar{x}_e + \hat{x}_e \cot\{4\pi f_e t + \phi_F\}. \tag{11}$$

The mean values $\bar{x}_0$ and $\bar{x}_e$ and the 'amplitudes' $\hat{x}_0$ and x_e of the time-dependent locations of forces result from integration of the local instantaneous pressures. As will

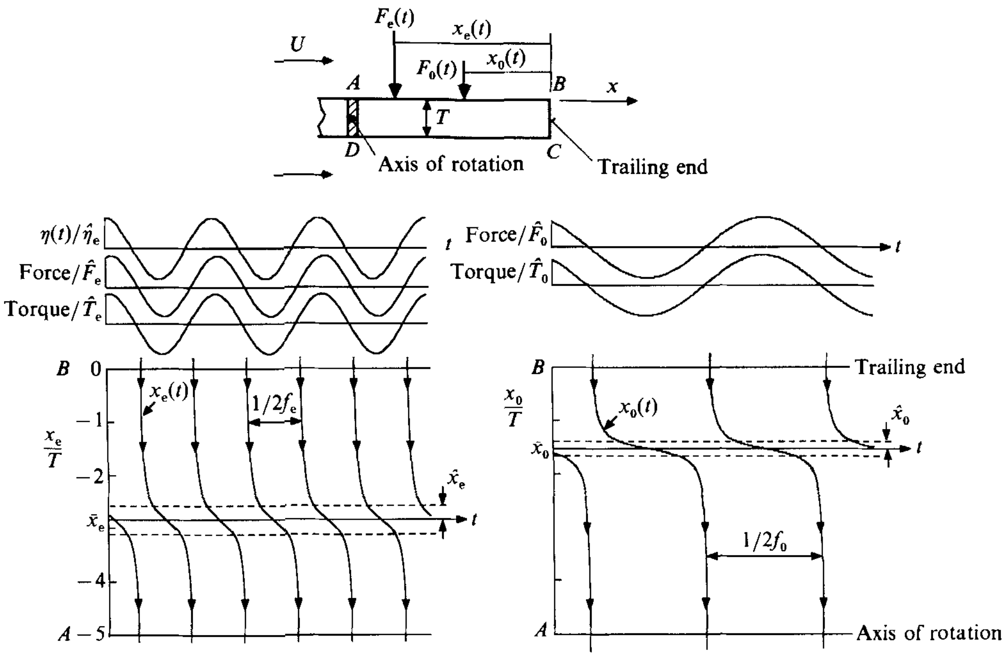

FIGURE 18. Force fluctuations and instantaneous locations of the points of application (both computed from integrated pressure distributions) for the components at the excitation frequency f_e and at the self-excited frequency f_0 (Parameters employed correspond to: $\hat{\eta}_e = 0.02, f_e/f_0^* = 2.05, f_e/f_0 = 2.18$).

be demonstrated, the points of application oscillate around their mean values according to the cotangent function, and the frequencies associated with the fluctuations $x_0(t)$ and $x_e(t)$ are $2f_0$ and $2f_e$ respectively.

7.2. *Representative variations of force location*

Figure 18 shows a typical example of time records of forces, torques and points of application for the components at the excitation frequency f_e and at the frequency f_0 of the self-sustained vortex formation. The chosen example shows a case of excitation above resonance where the amplitudes of the self-sustained pressure fluctuations $\hat{p}_0$ recover to amplitudes comparable with those in the case of the non-oscillating edge. The frequency ratio f_e/f_0 is 2.18; thus, the period of the self-sustained vortex shedding (graphs on the right) corresponds to a little more than two periods of the edge oscillation (graphs on the left). We observe a slight phase difference in the force and torque signals arising from the different weighting of the instantaneous pressure fluctuations along the edge surfaces when integrating force and torque.

In the schematic underneath the time records of force and torque of figure 18, the instantaneous points of application $x_e(t)$ and $x_0(t)$ of the respective forces are depicted. Twice per cycle, when the forces $F_e(t)$ and $F_0(t)$ pass through zero, $x_e(t)$ and $x_0(t)$ go to infinity, in accord with the cotangent function of (10) and (11).

7.3. *Force amplitude and phase shift*

Figure 19 displays the response characteristics of the force components as a function of non-dimensional excitation frequency f_e/f_0^* for the two values of displacement

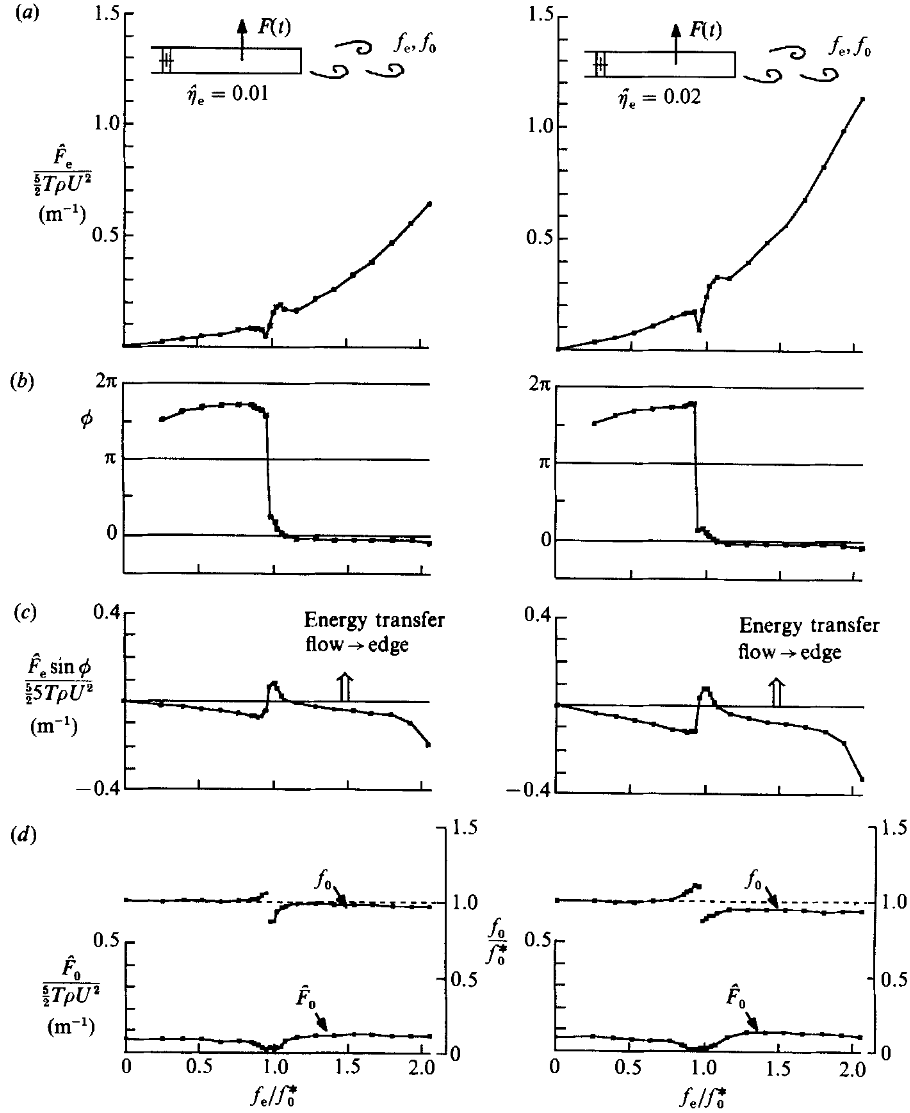

FIGURE 19. Response characteristics of the resultant loading upon the oscillating trailing edge showing: (*a*) amplitude of the force component $\hat{F}_e$ at the excitation frequency f_e; (*b*) phase angle ϕ of $F_e(t)$ relative to the displacement $\eta_0(t)$; (*c*) product $\hat{F}_e \sin\phi$ indicating the relative energy transfer; and (*d*) amplitude of the force component $\hat{F}_0$ at the self-excited frequency f_0 for $\hat{\eta}_e = 0.01$ (left) and $\hat{\eta}_e = 0.02$ (right).

$\hat{\eta}_e = 0.01$ and 0.02. The force magnitude $\hat{F}_e$, shown in figure 19(*a*) exhibits, for preresonant excitation ($f_e < f_0^*$) a decrease in amplitude, then a jump to higher values for resonant excitation. This transition is accompanied by a phase jump (figure 19*b*). For excitation above resonance ($f_e > f_0^*$), the value of the phase ϕ_F is nearly zero; this indicates the dominance of non-circulatory, or 'added mass', contributions to the force component at the frequency f_e. This is further confirmed by the fact that $\hat{F}_e$ increases as the square of the excitation frequency f_e and linearly with the displacement amplitude $\hat{\eta}_e$.

The phase ϕ_F in figure 19(*b*) indicates whether there is energy transfer from the

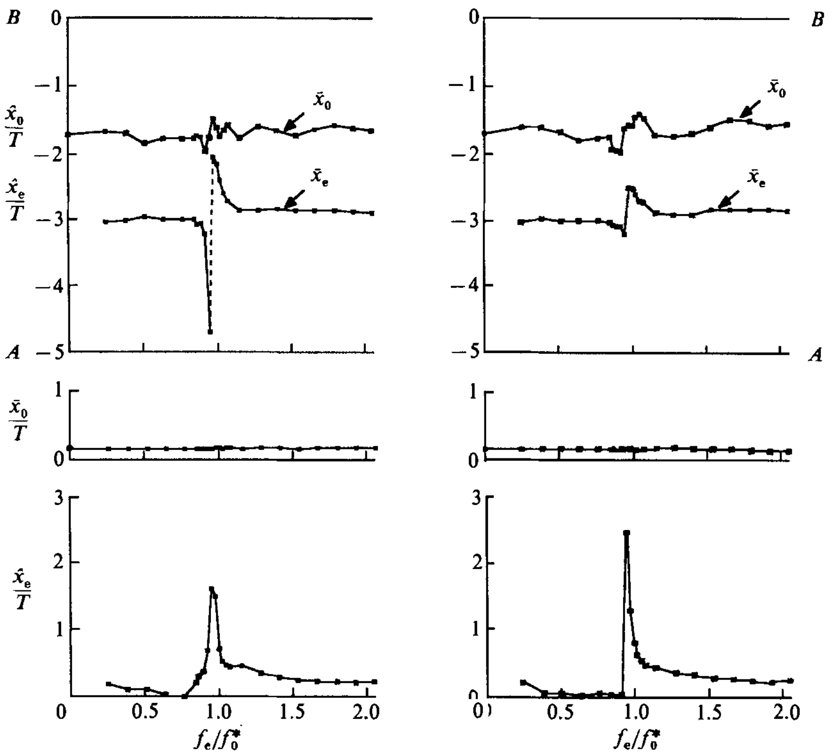

FIGURE 20. Mean (time-averaged) points of application $\bar{x}_0, \bar{x}_e$ and amplitudes $\hat{x}_0, \hat{x}_e$ of the resultant loading upon the oscillating trailing edge for $\tilde{\eta}_e = 0.01$ (left) and $\tilde{\eta}_e = 0.02$ (right).

fluid to the oscillating edge or vice versa. For the measurements shown, there is positive energy transfer from the flow to the edge in the range of $\pi > \phi_F > 0$.

The magnitude of this energy transfer follows from the product of $\hat{F}_e$ and $\sin \phi_F$ which is displayed in figure 19(*c*). This product can be considered as a force component that is in-phase with the velocity of the trailing-edge oscillations. There is only a narrow range near $f_e/f_0^* = 1$ where there is positive energy transfer from the fluid to the edge. In this range, there is the possibility of self-excited, fluidelastic oscillations of the corresponding, elastically mounted trailing edges.

In figure 19(*d*), the frequency f_0 and the force component $\hat{F}_0$ are displayed as a function of the normalized excitation frequency f_e/f_0^*. For excitation frequencies close to resonant excitation ($f_e = f_0^*$), the amplitudes of $\hat{F}_0$ are attenuated and the frequency f_0 departs significantly from the excitation frequency f_e. For larger amplitudes $\tilde{\eta}_e$ than those investigated here, however, we can expect a quenching of the force component $\hat{F}_0$ down to a level where $\hat{F}_0$ disappears in the noise level of the measurements which was at about 5% of $\hat{F}_e$; such quenching is reported by Staubli (1987) for similar cases of externally excited flow oscillators. Only for vanishing force component $\hat{F}_0$ is it correct to talk about a synchronization range; for the measurements presented herein, no complete synchronization occurs for external excitation at $f_e/f_0^* \approx 1$.

Figure 20 shows the computed points of application x_e and x_0 of the corresponding forces $\hat{F}_e$ and $\hat{F}_0$. The mean (time-averaged) value $\bar{x}_0$ of the self-sustained component shows considerable scatter near resonant excitation; this scatter may be due to measurement errors, which are relatively large in the range of excitation near

$f_e/f_0^* = 1$ because the associated force $\hat{F}_0$ and the pressure fluctuations $p_0(x,t)$ are almost completely quenched. However, the 'amplitude' $\hat{x}_0$ of the fluctuating point of application remains remarkably independent of the frequency ratio f_e/f_0^*. In contrast, the mean value $\bar{x}_e$ and the 'amplitude' $\hat{x}_e$ of the point of application associated with the force component $\hat{F}_e$ undergo significant changes with f_e/f_0^*. These changes have their origin in the fact that the streamwise phase gradient of the pressure field changes sign when the excitation passes through resonance, $f_e/f_0^* \approx 1$ (see figure 10). The consequence of this change in sign is that the computed torque fluctuations lag the force fluctuations for subresonant excitation while the torque leads the force for excitation above resonance. For torque fluctuations that are precisely in-phase with the force fluctuations, we expect singular behaviour of the point of application, which can actually be observed for the change from preresonant to resonant excitation; the mean value $\bar{x}_e$ becomes undefined and the 'amplitudes' $\hat{x}_e$ grow to very large values.

8. Summary

The flow structure of the near-wake region and the unsteady pressure field in the trailing-edge region are directly related to one another. To provide well-defined flow conditions at separation, a fully turbulent boundary layer was generated at the trailing edge. Even when the edge is stationary, there emerge highly organized vortical structures, which form periodically at frequency f_0^*. Spectral analysis of the fluctuations on the edge surface near the trailing end show that the non-deterministic, broadband contributions to the spectra were only a few percent of the contributions due to vortex formation. This emergence of highly organized flow structures from the fully turbulent flow at separation strongly suggests existence of an absolute, as opposed to a convective, instability in the near-wake region (Monkewitz & Nguyen 1987). In essence, the concept of the absolute stability mechanism is that a mechanism of self-forcing can exist in the near wake. These observations contrast with those of convectively unstable flows where external forcing is required to attain organized vortical structures in the presence of a turbulent boundary layer at thin trailing edges (Fiedler & Mansing 1985). We also note here earlier investigations of blunt-trailing-edge flows in which spectra indicating a highly organized near wake were obtained at relatively high Reynolds number (Graham & Maull 1971; Blake 1984*a*, *b*).

The flow structure of the near wake in the presence of perturbations of the trailing edge shows that for the range of synchronization ($f_e/f_0^* \approx 1$), the coherence of the near-wake vortex formation is somewhat enhanced, and formation of the vortices occurs closer to the trailing end. This observation is suggested by comparison of the flow visualization of figure 4 (stationary edge; $f_e/f_0^* = 0$) with that of figure 15 ($f_e/f_0^* = 1.02$) where the formation region is shorter and more hydrogen bubbles are concentrated within the vortex cores indicating enhanced concentration of vorticity. It substantiates the interpretation of velocity measurements of Graham & Maull (1971), who found that the rate of development, the coherence, and the spanwise correlation of vortex shedding were all increased for synchronization. Most important for our considerations here, however, is the nature of the near-wake flow structure when the excitation frequency is $f_e/f_0^* \neq 1$. At excitation below resonance ($f_e/f_0^* < 1$), the flow field is dominated (with some degree of modulation) by the self-sustained 'natural' vortex shedding at f_0. On the other hand, at excitation very near and above resonance, the flow field immediately behind the trailing end is dominated by the vortex shedding at the excitation frequency f_e. However, irrespective of the excitation conditions, the downstream wake rapidly 'recovers' to the frequency f_0 of the vortex street.

Regarding the phase of the vortex formation with respect to the motion of the oscillating edge, visualization of the vortex development shows that there are substantial changes in this phasing as synchronization or resonance is approached. At $f_e/f_0^* = 1$ it appears that vortex formation from the lower corner of the edge (see figure 15) first becomes pronounced when the trailing end has its maximum downward velocity (i.e. zero displacement: $\eta(t) = 0$). However, small changes in excitation frequency away from $f_e/f_0^* = 1$ produced substantial changes in phase shift of the vortex formation process. A limiting case of this phase shift occurs when there is subharmonic excitation at $f_e = 0.5f_0^*$. In this case, the vortex formation can be observed at the lower corner when the edge is in the uppermost position, and half a cycle later from the lower corner when the edge is in its lowest position. An analogous type of vortex formation of the self-sustained vortices occurs at $f_e/f_0^* = 2$.

Determination of the instantaneous pressure distribution along the surface of the trailing edge has revealed several important features. First, irrespective of frequency of excitation, including the limiting case of the stationary edge, maximum amplitude of the pressure fluctuation occurs at or very near the corner of the edge. Consequently, application of a Kutta condition is indeed inappropriate, since the pressure amplitude would have to go gradually to a value of zero as the corner of the edge is approached. Instead, modelling of this trailing-end (or corner) region should focus on a singular-type behaviour there. When the edge undergoes oscillations, the region upstream of the corner is dominated by the non-circulatory or 'added mass' contribution to the fluctuating pressure; on the other hand, as the corner of the edge is approached, the circulatory or 'vortex-induced' contribution of the pressure becomes important. This circulatory contribution to the pressure is confined to a region within about one trailing-edge thickness from the corner, corresponding to approximately one half-wavelength of the vortex street formed from the edge. It is this highly localized concentration of the circulatory pressure contribution that determines the sign (plus or minus) and amplitude of the energy transfer between the edge and the fluid surrounding it.

Three-dimensional portrayals of the streamwise variation of the amplitude and phase of the pressure fluctuations, as a function of the excitation frequency of the trailing edge, show several important characteristics. As the frequency ratio f_e/f_0^* approaches a value of 1, that is within the range of synchronization, the amplitude of the pressure $\hat{p}_e$ at the excitation frequency shows a resonant peak, while that of the self-excited component $\hat{p}_0$ is attenuated or 'quenched'. As noted in the foregoing, this resonant behaviour of the $\hat{p}_e$ component is localized at the corner and is due to the increased circulatory contribution to $\hat{p}_e$. The phase of the fluctuating pressure $p_e(x,t)$ shows substantial gradients in the streamwise direction as the corner of the edge is approached. Particularly important is the fact that this phase gradient changes sign as the excitation frequency passes through the synchronization range for $f_e/f_0^* \approx 1$. That is, the phase decreases in the direction of flow for $f_e/f_0^* < 1$, while it increases in the direction of flow for $f_e/f_0^* > 1$. A further feature of these phase distributions is that there is an abrupt change in phase or a phase jump for resonant excitation at $f_e/f_0^* \approx 1$. The magnitude of this phase jump varies with streamwise location (x/T) owing to the changing ratio of circulatory and non-circulatory contributions to the pressure fluctuations with streamwise location.

All of these details of the pressure field provide a basis for understanding the changes in gross loading observed with changes of excitation frequency as described in the variety of investigations noted in the Introduction. For example, the region of the circulatory contribution to the fluctuating pressure near the corner of the trailing edge solely determines the phase shift of the force (lift) acting on the edge with respect to the displacement of the edge. This phasing of force with respect to displacement determines the direction of energy transfer between the edge and the surrounding fluid. Based on integrations of the instantaneous surface pressure, it has been found that a local maximum of energy transfer from the edge to the flow occurs for preresonant excitation, i.e. for excitation at frequencies near the onset of the phase jump (see figure 19*b*). In contrast, the maximum energy transfer from the flow to the edge occurs for the second part of the phase shift, which occurs at resonant excitation. In this range of excitation frequencies, where there is positive energy transfer from the flow to the edge, self-excited fluidelastic oscillations of trailing edges can be expected.

Integration of the instantaneous surface pressure distributions determines the instantaneous point of application of the force on the surface of the edge. In determining this location, it is necessary, of course, to consider both the moment and the force on the edge. As described in the foregoing, the sign of the streamwise phase gradient of the surface pressure changes when going from below to above $f_e/f_0^* = 1$. This change in sign of the phase gradient is reflected in the evaluation of the force and torque: consequently, it is also reflected in the instantaneous point of application of the force at each value of excitation frequency. For subresonant excitation ($f_e/f_0^* < 1$), the torque fluctuation (defined with respect to the axis of rotation) lags the force fluctuation. On the other hand for excitation above resonance ($f_e/f_0^* > 1$), the inverse occurs. For resonant excitation at $f_e/f_0^* \approx 1$, where there is a jump in phase angle between the force on the edge and the displacement of the edge, the point of application of the force shows a singular behaviour.

Consideration of the instantaneous pressure fields has also led to comparison of the instantaneous location of the force components at both frequencies f_e and f_0. It is demonstrated that the points of application of the respective forces oscillate around their mean values in accordance with a cotangent function. The time-mean location of the force component at the edge perturbation frequency f_e undergoes an abrupt jump – by as much as two trailing-edge thicknesses – as the synchronization range is approached. This large jump in the time-mean force location is accompanied by large amplitude fluctuations in its location of the order of two trailing-edge thicknesses. These changes are associated with the fact that the streamwise phase gradient of the surface pressure field changes on passing through the synchronization range. In contrast, the location of the force component at the self-excited frequency f_0 of vortex formation shows insignificant variations as the excitation frequency varies.

The aim of this investigation has been to provide a physical basis for the understanding of vortex-induced loads at trailing edges of vibrating plates. Details of the instantaneous surface pressure field defined in the foregoing, such as regions where non-circulatory and circulatory contributions to the pressure are dominant, the location and magnitude of phase jumps in the fluctuating pressure, occurrence of streamwise phase gradients of the pressure field, and the relationship of these details to the instantaneous flow structure provide insight into the factors that determine the overall lift force on the oscillating edge.

The stay of T. Staubli at Lehigh University was made possible by a grant from the Swiss National Science Foundation. Major project funding was provided by the Office of Naval Research and supplemental funding was received from the National Science Foundation. Certain aspects of the flow visualization were supported by the Volkswagen Foundation.

REFERENCES

ABERNATHY, F. & KRONAUER, R. E. 1962 The formation of vortex streets. *J. Fluid Mech.* **13**, 1–20.

ARCHIBALD, F. S. 1975 Unsteady Kutta condition at high values of the reduced frequency parameter. *J. Aircraft* **12**, 545–550.

BEARMAN, P. W. 1967 On vortex street wakes. *J. Fluid Mech.* **28**, 625–641.

BEARMAN, P. W. 1984 Vortex shedding from oscillating bluff bodies. *Ann. Rev. Fluid Mech.* **16**, 195–222.

BEARMAN, P. W. & CURRIE, I. G. 1979 Pressure fluctuation measurements on an oscillating circular cylinder. *J. Fluid Mech.* **91**, 661–677.

BEARMAN, P. W. & OBASAJU, E. D. 1982 Vortex shedding from bluff bodies in oscillatory flow. *J. Fluid Mech.* **99**, 225–245.

BERGER, E. & WILLE, R. 1972 Periodic flow phenomena. *Ann. Rev. Fluid Mech.* **4**, 313–340.

BISHOP, R. E. D. & HASSAN, A. Y. 1964 The lift and drag forces on a circular cylinder oscillating in a flowing fluid. *Proc. R. Soc. Lond.* A **277**, 51–75.

BISPLINGHOFF, E. H., ASHLEY, H. & HALFMAN, R. L. 1955 *Aeroelasticity*. Addison Wesley.

BLAKE, W. K. 1984 Trailing edge flow and aerodynamic sound: Part 1, Tonal pressure and velocity fluctuations. *David W. Taylor Naval Ship research and Development Center, Rep.* DTNSRDC-83/113.

BLAKE, W. K. 1984 Trailing edge flow and aerodynamic sound: Part 2, Random pressure and velocity fluctuations. *David W. Taylor Naval Ship Research and Development Center, Rep.* DTNSRDC-83/113.

BLAKE, W. K. & MAGA, L. J. 1979 Near wake structure and unsteady pressures at trailing edges of airfoils. *Proc. Joint IUTAM/ICA/AIAA Symposium on Mechanics of Sound Generation in Flows* (ed. E.-A. Mueller), pp. 69–75. Springer.

BREPSON, R. & LEON, P. 1972 Vibrations induced by von Kármán vortex trail in guide vanes. *IUTAM-IAHR Symp. Karlsruhe 1972, Flow-Induced Vibrations* (ed. E. Naudascher), pp. 318–332. Springer.

FENG, C. C. 1968 The measurement of vortex-induced effects on flow past stationary and oscillating circular and D-section cylinders. M.A.Sc. thesis, University of British Columbia.

FIEDLER, H. E. & MANSING, P. 1985 The plane turbulent shear layer with periodic excitation. *J. Fluid Mech.* **150**, 281–309.

GERRARD, J. H. 1978 The wakes of cylindrical bluff bodies at low Reynolds number. *Phil. Trans. R. Soc. Lond.* A **288**, 351–389.

GRAHAM, J. M. R. & MAULL, D. J. 1971 The effects of an oscillating flap and an acoustic resonance on vortex shedding. *J. Sound Vibr.* **18**, 371–380.

GREENWAY, M. E. & WOOD, C. J. 1973 The effect of a bevelled trailing edge on vortex shedding and vibration. *J. Fluid Mech.* **61**, 323–335.

GRIFFIN, O. M. & RAMBERG, S. E. 1974 The vortex-street wakes of vibrating cylinders. *J. Fluid Mech.* **66**, 553–576.

JOHANSEN, J. B. & SMITH, C. R. 1983 The effects of cylindrical surface modifications on turbulent boundary layers. Rep. FM-3, Lehigh University, Department of Mechanical Engineering & Mechanics, Bethlehem, PA 18015.

KOCH, W. 1985 Local instability characteristics and frequency determination of self-excited wake flows. *J. Sound Vibr.* **99**, 53–83.

MAIR, W. A. & MAULL, D. J. 1971 Bluff bodies and vortex shedding – a report on Euromech 17. *J. Fluid Mech.* **45**, 209–224.

MONKEWITZ, P. A. & NGUYEN, L. M. 1987 Absolute instability in the near-wake of two-dimensional bluff bodies. *J. Fluids Structures* **1**, 165–184.

MORKOVIN, M. 1964 Flow around circular cylinder – a kaleidoscope of challenging fluid phenomena. *Proc. ASME Symposium on Fully Separated Flows, Philadelphia*, pp. 102–118.

ONGOREN, A. & ROCKWELL, D. 1988 Flow structure from an oscillating cylinder. Part 1. Mechanisms of phase shift and recovery of the near-wake. *J. Fluid Mech.* **191**, 197–223.

PURTELL, L. P. & KLEBENOFF, P. S. 1981 Turbulent boundary layer at low Reynolds number. *Phys. Fluids* **24**, 802–811.

ROSHKO, A. 1954 On the drag and shedding frequency of two-dimensional bluff bodies. *NACA Tech. Note* 3169.

SAFFMAN, P. G. & SCHATZMAN, J. C. 1982 An inviscid model for the vortex street wake. *J. Fluid Mech.* **122**, 467–486.

SARPKAYA, T. 1978 Fluid forces on oscillating cylinders. *J. Waterway, Port, Coastal Ocean Engng Div. ASCE* **104**(WW4), 275–290.

SARPKAYA, T. 1979 Fluid forces on oscillating cylinders, a selective review. *Trans. ASME* E: *J. Appl. Mech.* **26**, 241–258.

SCHEWE, G. 1983 On the structure and resolution of wall-pressure fluctuations associated with turbulent boundary-layer flow. *J. Fluid Mech.* **134**, 311–328.

SCHLICHTING, H. 1979 *Boundary Layer Theory*. McGraw-Hill.

STAUBLI, T. 1981 Calculation of the vibration of an elastically mounted cylinder using experimental data from a forced oscillation. In *ASME Symp. on Fluid–Structure Interaction in Turbomachinery*, pp. 19–24.

STAUBLI, T. 1983 Untersuchung der oszillierenden Kräfte am querangeströmten, schwingenden Kreiszylinder. Dissertation ETH 7322.

STAUBLI, T. 1987 Entrainment of self-sustained flow oscillations: phase-locking or asynchronous quenching? *Trans. ASME* E: *J. Appl. Mech.* **54**, 706–712.

UNAL, M. F. & ROCKWELL, D. 1988 On vortex formation from a cylinder. Part 1. The initial instability. *J. Fluid Mech.* **190**, 491–512.

WOOD, C. J. 1971 The effect of lateral vibrations on vortex shedding from blunt-based aerofoils. *J. Sound Vib.* **14**, 91–102.

ZDRAVKOVICH 1982 Modification of vortex shedding in the synchronization range. *Trans. ASME* I: *J. Fluids Engng*, **104**, 513–517.